nature COMMUNICATIONS

ARTICLE

https://doi.org/10.1038/s41467-021-25875-y OPEN

Complex small-world regulatory networks emerge from the 3D organisation of the human genome

C. A. Brackley [1], N. Gilbert [2], D. Michieletto[1,2], A. Papantonis[3], M. C. F. Pereira[1], P. R. Cook [4] & D. Marenduzzo [1✉]

The discovery that overexpressing one or a few critical transcription factors can switch cell state suggests that gene regulatory networks are relatively simple. In contrast, genome-wide association studies (GWAS) point to complex phenotypes being determined by hundreds of loci that rarely encode transcription factors and which individually have small effects. Here, we use computer simulations and a simple fitting-free polymer model of chromosomes to show that spatial correlations arising from 3D genome organisation naturally lead to stochastic and bursty transcription as well as complex small-world regulatory networks (where the transcriptional activity of each genomic region subtly affects almost all others). These effects require factors to be present at sub-saturating levels; increasing levels dramatically simplifies networks as more transcription units are pressed into use. Consequently, results from GWAS can be reconciled with those involving overexpression. We apply this pan-genomic model to predict patterns of transcriptional activity in whole human chromosomes, and, as an example, the effects of the deletion causing the diGeorge syndrome.

[1] SUPA, School of Physics and Astronomy, University of Edinburgh, Peter Guthrie Tait Road, Edinburgh EH9 3FD, UK. [2] MRC Human Genetics Unit, MRC Institute of Genetics & Molecular Medicine, University of Edinburgh, Western General Hospital, Edinburgh EH4 2XU, UK. [3] Institute of Pathology, University Medical Center, Georg-August University of Göttingen, 37075 Göttingen, Germany. [4] Sir William Dunn School of Pathology, University of Oxford, South Parks Road, Oxford OX1 3RE, UK. ✉email: dmarendu@ph.ed.ac.uk

Transcription—the copying of DNA into RNA—is tightly regulated. Early insights into regulatory mechanisms came from work on binary on/off genetic switches controlled by one or just a few transcription factors such as the lambda and lac repressor in *Escherichia coli*[1]. Similar regulatory mechanisms are present in eukaryotes, albeit with additional complexity. For instance, a fibroblast cell can be reprogrammed into a muscle cell by a single master regulator (MYOD)[2,3] or into pluripotent stem cells by four Yamanaka factors (Oct4, Sox2, c-Myc, Klf4)[4].

Genome-wide association studies (GWAS) lead to quite a different view: gene regulation is widely distributed and involves interactions between hundreds (perhaps thousands) of loci scattered around the genome[5,6]. GWAS allow quantitative trait loci (QTLs) affecting any measurable genetic trait to be ranked in an unbiased way. With complex traits like human height, and diseases such as schizophrenia and type II diabetes, the top ten QTLs in the rank order combine to yield only modest effects, while the top one-hundred still account for less than half of the total genetic effect. Hundred more QTLs are expected to be identified as sample sizes and data resolution improve[5–7]. Expression QTLs (eQTLs) are QTLs affecting transcription of other DNA regions. Perhaps surprisingly, these are rarely found in genes encoding transcription factors or other proteins; instead, they usually involve single-nucleotide changes in non-coding elements that bind transcription factors such as active enhancers and promoters[8–10].

Results from GWAS lead to the view that most gene-regulatory networks are incredibly complex, with the activity of a given gene being affected by a panoply of eQTLs, each having a tiny effect. This is captured by the "omnigenic" model, which is based on a set of gene-interaction equations[5,6] such that the activity of almost any gene affects that of almost every other one. This model provides a useful and appealing framework to view GWAS results. However, it is difficult to compare its outputs with experimental data because it contains many parameters that are currently unknown and require fitting to training datasets.

In general, existing models for gene regulation traditionally assume post-transcriptional and biochemically mediated interactions between different genes[11,12], and disregard the role of three-dimensional (3D) chromatin structure. Here we propose an alternative but complementary framework that links transcriptional regulation directly to 3D genome structure, deliberately neglecting downstream biochemical regulation to enable unambiguous interpretation of our results. This framework is motivated by experiments showing that chromatin folding can lead to contacts between enhancers and promoters affecting transcription, and that 3D structure changes in disease[13,14]. Additionally, because our modelling is essentially fitting-free, its output can be directly compared to experiments. When the agreement is good, our model is validated; when poor, it points to some missing ingredient (such as biochemical feedback) that could be included in future models.

We use stochastic computer simulations of a polymer model for chromosome organization, in which a chain of beads represents a chromatin fibre, and a set of spheres complexes of transcription factors and RNA polymerases—which we will call "TFs" for short. Some chromatin beads are identified as transcription units (TUs), and we call them TU beads. They contain binding sites for TFs, and can be sites of transcriptional initiation (we do not discriminate between genic and non-genic promoters). As a simple starting point we only consider one type of TF that binds specifically and multivalently to TU beads, and non-specifically (i.e., with weak affinity) to every other bead. We perform 3D Brownian dynamics simulations that evolve the diffusive dynamics of the chain and associated factors. We previously showed that similar polymer models yield structures resembling those seen using chromosome–conformation–capture (3C)[15–19] and microscopy[20]. Here, we link 3D structure to expression and transcriptional dynamics by measuring how often a TU bead is transcribed—which we do by computing the fraction of time it binds a TF. To establish the methodology, we model a 3 Mbp chromatin fragment, before going on to simulate whole human chromosomes.

Our simulations capture many features of eukaryotic regulation. For example, transcription is stochastic and bursty (in agreement with single-cell transcriptomics data), and the predicted pattern of transcriptional activity in human chromosomes correlates significantly with that observed experimentally. We also find that small-world (percolating) networks that encapsulate much of the rich complexity observed in GWAS emerge through spatial effects alone. In other words, the activity of most (probably all) TUs in our model is affected by the activity of most (probably all) other segments in the genome. We find such pan-genomic regulation critically requires non-saturating concentrations of TFs—as normally found in vivo—and that increasing concentrations dramatically simplifies the networks. This enables us to reconcile the GWAS-based view that regulatory networks are complicated with the observation that overexpressing one or a few TFs can decisively alter cell state.

Results

We first consider a simple system where a 3 Mbp chromatin fragment is represented by a chain of 1000 beads (each 30 nm in diameter, and corresponding to 3 kbp). We select at random $N = 39$ beads and identify them as TUs (Fig. 1a; see "Methods" and Supplementary Note 1 for more details). The linear density of TUs in the fragment is similar to that in human chromosome 22. Additionally, n spheres (also 30 nm in diameter) represent TFs (recall these are complexes of transcription factors and RNA polymerase II). TFs bind reversibly to TUs via a strong attractive interaction, and to all other beads weakly and non-specifically. An important feature is that TFs switch between active (binding) and inactive (non-binding) state at rate α. Many factors switch like this in vivo (e.g., due to phosphorylation and de-phosphorylation), and switching is required to account for the rapid exchange of factors and polymerases between bound and free states seen in live-cell photobleaching experiments[21]. As ~7 out of 8 polymerases attempting to initiate at promoters dissociate with a half-life of ~2.4 s[22], our complexes generally behave like those in vivo.

While our results refer to a single patterning of TUs along the fibre, they are representative of any arbitrary random positioning of TUs: in other words the qualitative trends we present below are robust and do not depend on the particular choice of the 1D pattern of TUs along the fibre in any way.

We say a TU bead is transcribed whenever a TF lies close to it (see "Methods"), and the transcriptional activity of a TU is then the fraction of time it is transcribed during a simulation. To reflect the situation in mammalian cells (Supplementary Note 3 and ref. [23]), we typically assume there are fewer TFs than TU beads (i.e., $n = 10$ TFs in the active binding state at any time, compared to 39 TUs).

By interrogating TF-chromatin interactions at regular time intervals over hundreds of simulations, we build up a population picture of transcription. A typical configuration of the 3 Mbp fragment is shown in Fig. 1B. Strikingly, bound TFs spontaneously cluster, despite there being no attractive interactions between TUs or between TFs. Such clustering is driven by the "bridging-induced attraction"[16,24,25] that arises due to a positive feedback: when a TF forms a molecular bridge between two chromatin regions and forms a loop, the local chromatin concentration increases, making further TF binding more likely. Clusters then grow until limited by entropic costs of crowding

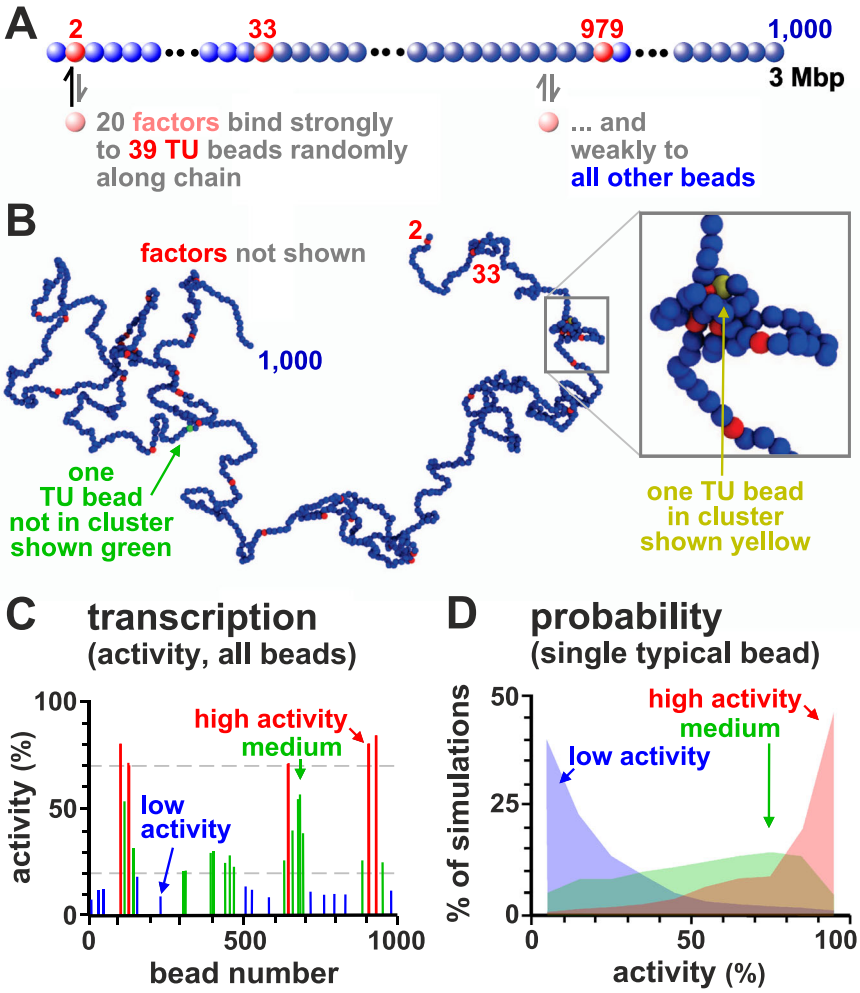

Fig. 1 Patterns of transcriptional activity. A Schematic of the model. Twenty TFs (pink) that switch between on/off states at rate $\alpha = 10^{-5}\tau_B^{-1}$ (with τ_B the Brownian time, see "Methods") or $0.001\,s^{-1}$ bind specifically to 39 TUs (red beads) randomly positioned along the chain, and non-specifically to other beads (blue). A TU is considered transcriptionally active if associated with a TF. **B** Example conformation (TFs not shown). Some beads cluster and form loops; one TU not in a cluster (and not transcribed) is green, and another that is in a cluster (and transcribed) is yellow. Inset: zoom of boxed region. **C** Transcriptional activity for each TU bead averaged over 1000 simulations (each lasting $10^5\tau_B$). TUs are grouped according to activity, with red, green, and blue bars showing high (>70%), medium (20–70%) and low (<20%) activity, respectively. This gives a population-level measure of activity. **D** Variation of activity across simulations (reflecting cell-to-cell variation) for three representative TUs with high (red), medium (green), or low (blue) average activity (defined as in **C**).

(Fig. S1A). Most of the non-trivial phenomena described below result from such clustering. Clustering requires TF multivalency, as monovalent factors do not cluster[24]. However, the assumption of multivalency, which is common in the polymer physics literature[15], is well-founded. Several TFs are known to be bivalent or multivalent[26], and, more importantly, our spheres represent complexes of TFs and polymerases, so they will behave as multivalent binders even when the individual TFs in the complex are monovalent. Although clustering does not require any interactions between TFs, adding a weak attraction between them, as might arise for instance due to macromolecular crowding or electrostatic interactions between intrinsically disordered regions, should not qualitatively change any of the results discussed here (at least as long as TFs still microphase separate into clusters rather than undergoing macroscopic phase separation).

The clusters we observe, and which emerge through the bridging-induced attraction, are qualitatively similar to those seen in vivo, which are variously described as transcriptional compartments, hubs, super-enhancer (SE) clusters, phase-separated droplets/condensates, and factories[7,10,27–29]. They are also similar to the contact domains seen in microC[30], which are formed by accessible DNA sites clustering together in 3D space. Clustering arising through the bridging-induced attraction has recently been found in vitro for systems of DNA and cohesin (which binds multivalently to DNA)[31].

Transcriptional activity varies along the chromatin fibre and is highly stochastic. As TFs have the same affinity for all TUs, one might expect each TU to be bound with equal likelihood; however, transcriptional activity (the fraction of time a TU is transcribed) varies from ~10–90% (Fig. 1C). What causes this variation? As TF copy number is limiting, and as bound TFs cluster, most transcription occurs in clusters—as is the case in vivo[7,32–34]. Since TUs are positioned irregularly along the fragment, some have closer neighbours in 1D sequence space than others, and these are inevitably the ones most likely to cluster and be transcribed. Instead, those far from their neighbours are less likely to cluster and are less active. Accordingly, the transcriptional activity of a TU anticorrelates with distance to the nearest TU along the fibre (Fig. S1B; the Spearman correlation is $r \simeq -0.94$, p value $p < 10^{-12}$).

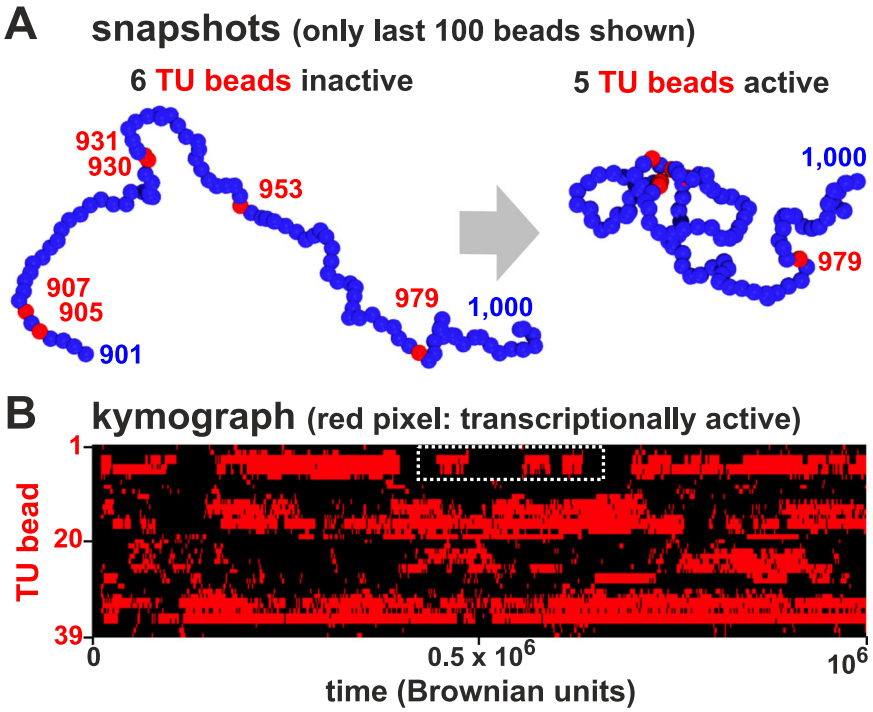

Fig. 2 Transcriptional bursting. A Snapshots showing a 100-bead section of the simulated chain taken at different times. Initially, none of the 5 TUs (red) are in clusters and they are all inactive; later, 4 TUs join a cluster and are close to TFs—and so are transcribed. **B** Kymograph where each row shows the changing transcription state of one TU during a simulation; pixels are colored red if the bead is associated with a TF and so transcribed, or black otherwise. White rectangle: example of bursts.

While Fig. 1C pertains to population averages of 1000 simulations, it is informative to consider each simulation independently (as in single-cell transcriptomics). Such analysis shows that transcriptional activity is stochastic, varying substantially from simulation to simulation: a TU active in some simulations may be silent in others (Fig. 1D).

Transcriptional bursting. During a simulation, chromatin conformation can change dramatically (Fig. 2A). Such changes often yield transcriptional "bursts"—periods of continued activity followed by silent periods (Fig. 2B)—as TUs with intermediate levels of activity repeatedly join a cluster to give a burst and then dissociate. Notably, TUs lying close to each other in sequence space often start and stop bursts coordinately due to the intrinsic positive feedback in the system (Fig. S1A).

These results are consistent with experimental observations: single cell Hi-C[35] and transcriptomics[36] show that the structure and function of each individual cell is unique, and bursting is well documented[37–40] with nearby promoters often firing together[38].

Local chromatin architecture creates small-world percolating transcription networks. To investigate correlations between transcriptional activities of different TUs, we compute the Pearson correlation matrix between the activities of all possible TU pairs, and identify an emergent regulatory network in which TUs form nodes (Figs. 3A and S2). Specifically, we draw an edge between two TUs whenever there is a statistically significant positive or negative correlation between their transcriptional dynamics (Fig. 3A). This network arises only due to spatial interactions, as we assume no underlying biochemical regulation.

The network shows a striking property. With $n = 10$ active TFs, most nodes are connected (Fig. 3Aii), and the fraction of TUs participating in the largest connected component is close to 1 (Fig. 3B). Such a network is said to be "percolating", which means that any two nodes are connected by a path along edges. Our percolating networks are also "small-world", which means that most nodes can be reached from every other node by a small number of steps[41]—we provide quantitative measurements of the small world-ness of our networks in the SI (Supplementary Note 4). The small-world phenomenology is consistent with the multitude of small-effect eQTLs detected by GWAS[5,6]. Notably, the regulation we observe acts at the transcriptional level, and not post-transcriptionally as envisaged by the omnigenic model[5,6].

How might our simple model give rise to complex regulatory networks? By analysing simulation trajectories, we noted that TUs lying near each other in 1D sequence space often joined the same cluster in 3D. As a result, the activity of these clustered beads is highly positively correlated. At the same time, cluster formation sequesters TFs and so reduces the likelihood that another cluster forms elsewhere. As a result, most long-range correlations are negative (Fig. 3A).

Crucially, these network properties depend on there being a low TF copy-number (as in vivo[23]) so TU beads do not become saturated. We therefore reasoned that increasing copy number should suppress correlations as more rarely transcribed TUs are pressed into use. Indeed, increasing n reduces long-range negative correlations (Fig. 3Aiii,iv), and the fraction of nodes in the largest-connected component falls (Fig. 3B). Another way to think about this result is: if resources are plentiful, there is no need for sharing or competition, and all TUs can bind a TF independently of each other. If TFs do not switch and are permanently in the binding state (and $n = 10$), the network becomes even more highly connected (Fig. 3Ai).

Modelling effect of mutations and SNPs in regulatory elements. GWAS reveals that single-nucleotide polymorphisms (SNPs) in regulatory elements and TUs can lead to many small changes in transcriptional activity across the genome. To model

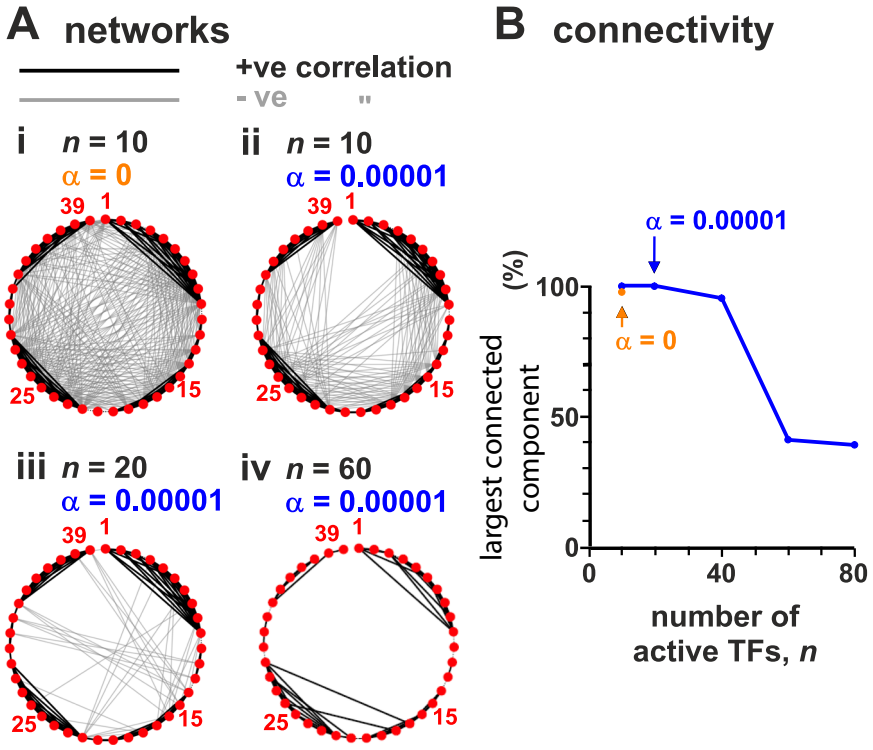

Fig. 3 Regulatory networks formed by TU beads are percolating at low TF concentrations. Simulations (as Fig. 1, with ≥800 simulations/condition) with different average numbers of active TFs (n) and switching rate (α). Networks were constructed by calculating the Pearson correlation between the transcription time series for all pairs of TUs; nodes represent each of the 39 TUs and edges are placed between nodes where there is a significant correlation (>0.15 in absolute value, corresponding to $p < 10^{-6}$; two-sided Student's t-test). **A** Effect of TF concentration and switching. Thirty-nine nodes are shown around the perimeter, and thick black and grey lines denote positive and negative correlations between transcriptional activities of bead pairs. **B** Effect of n on the fraction of nodes in the largest connected component.

this, we abrogate TF binding to one TU in the chain. Bead 930 is chosen first because it is usually highly active (Fig. 1C). This single "knock-out" affects in a statistically significant way the activity of almost half of the other TUs, both near and far away in sequence space (Fig. 4Aii). The immediately adjacent TU (i.e., bead 931) is down-regulated the most, while more distant ones are up-regulated (due to loss of a strong competitor). This knock-out also rewires the whole network, even though it still retains its small-world character (Fig. 4Aiii). Both positive and negative interactions are affected along the whole chain, as shown by a heat map of the change in Pearson correlation between TU transcriptional activities (Fig. 4Aiv).

We next systematically knock out each TU in turn. To quantify global effects, we define a "transcriptional difference" between the wild type and each knock-out based on a standard Euclidian-distance metric (SI, Supplementary Note 2); the larger this quantity, the more different the two states are. This difference varies >10-fold between different mutations (Fig. 4Bi).

Together, these observations are reminiscent of the behaviour of SNPs and eQTLs. Thus, each TU mutant can be seen as a SNP underlying an eQTL; then, those with low and high transcriptional differences (Fig. 4Bi,ii) are low- and high-effect eQTLs (low-effect mutants are often isolated in sequence space), and those with wide effects (e.g., bead 930 in Fig. 4A) may be viewed as omnigenic.

Modelling loops, heterochromatin and euchromatin. In mammalian genomes, promoter-enhancer pairs are often contained in loops stabilized by cohesin and the CCCTC-binding factor (CTCF)[42–44]. To investigate how such loops might affect transcription, we incorporated eight permanent and non-overlapping loops at different positions in the chain (Fig. 5A, loops a–h). In reality, such loops may arise from extrusion by cohesin halted at convergent CTCF loops[42]. Our assumption of stable, permanent loops is quantitatively accurate in the limit in which the interaction between cohesin and CTCF is strong and long-lived. However, we expect the trends to be qualitatively similar for more transient loops consistent with the loop extrusion model as in refs. [19,43].

The inclusion of stable loops has subtle effects. For example, loop h encompasses three TUs (beads 905, 907, 930), and expression of one is slightly boosted compared to the unlooped case (Fig. 5B, C). This is consistent with the idea that looping switches on some genes during development[45], and can increase enhancer–promoter interactions[46,47]. However, up-regulation requires appropriate positioning of a TU within the loop. For instance, loop d encompasses two TUs (beads 396 and 404), and has no effect on their activity. Broadly speaking, looping up-regulates activity, but not invariably so, and—perhaps surprisingly—two of the three most up-regulated TUs (beads 33 and 886) are not contained in loops (Fig. 5C). Looping also extensively rewires the regulatory network (Fig. 5D, E). Globally, the increase in activity is modest, as incorporating all beads into closely packed loops only increases total activity by ~10%, with—once again—some TUs being down- as well as up-regulated (Fig. S3). This is consistent with experiments showing that the interplay between looping and expression is complex[48] but slight (e.g., knocking down human cohesin leaves expression of 87% genes unaffected, with global levels changing <30%[49]).

In simulations thus far, TFs bind strongly to TU beads, and weakly to all others to model binding to open euchromatin[19,50]. To

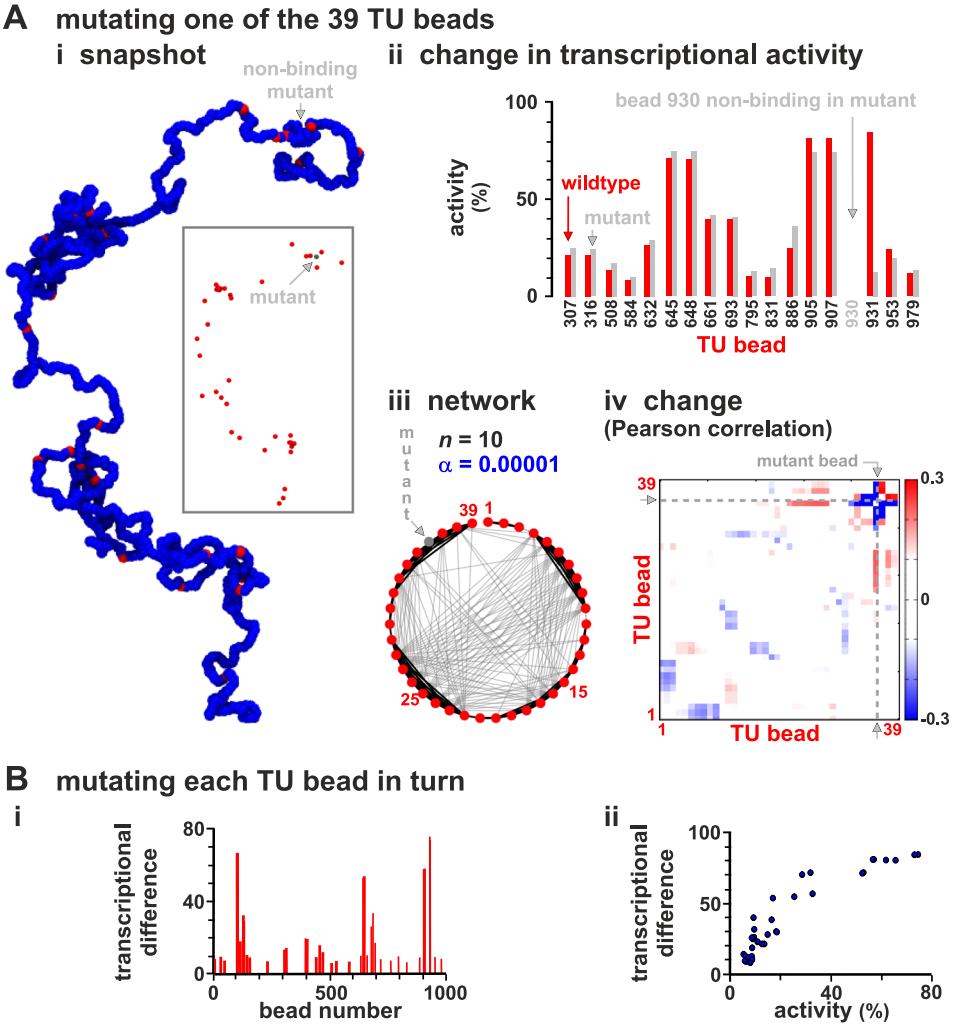

Fig. 4 Modelling SNPs and eQTL action. Sets of simulations (≥800 simulations/condition) where each of the 39 TU beads is made non-binding in turn (to represent 39 different SNPs in regulatory elements) are compared with those with the "wild-type" chain (as Fig. 1). **A** Chain with mutant (non-binding) TU bead 930. (i) Snapshot. TFs not shown (inset: same structure without blue beads). (ii) Transcriptional rates of the 17 TUs with significantly different values in mutant fibre compared with the wild-type one ($p \simeq 0.046$; two-sided Student's t-test). (iii) Regulatory network inferred from the matrix of Pearson correlations between activities of TUs. (iv) Change in Pearson correlation between TUs. **B** Results from simulations where each TU bead is mutated in turn, and the "transcriptional difference" from the wild type (see text and Supplementary Note 2) determined. (i) Transcriptional difference versus position along the chain. (ii) Positive correlation of transcriptional difference with TU activity in wild type. The plot shows that if we mutate a TU with high transcriptional activity, this leads to a larger difference.

investigate the effects of heterochromatin—which binds few TFs, carries few histone marks[51], and is gene poor and traditionally viewed as transcriptionally inert—we perform simulations where four of the most-active TUs (905, 907, 930, and 931) are embedded in a non-binding segment (running from bead 901–940). This has a dramatic effect (Fig. 6A–C): the activity of the TU beads now embedded in the non-binding island are at least halved, some nearby neighbors are down-regulated, and more distant ones up-regulated (again due to a reduction in competition; Fig. 6B, C). The regulatory network is also rewired (Fig. 5D, E).

Just as embedment in a non-binding segment down-regulates a TU bead, embedment in a weak-binding (euchromatic) one up-regulates it (Fig. S4). This shows our model effectively captures position effects where the local chromatin context strongly influences activity[52].

Modelling a whole human chromosome. We next model a whole mid-sized human chromosome (HSA 14, length 107 Mbp; Fig. 7A) in a well-characterized and differentiated diploid cell (HUVEC, human umbilical vein endothelial cell). Now, multivalent and switchable TFs (20% active at any moment) at a non-saturating concentration bind to a string with 35784 beads. As chromosome territories are often ellipsoidal, simulations are performed in an ellipsoid of appropriate size[7,53]; consequently, chromatin density is now higher than in simulations detailed above, with volume fractions comparable to those in vivo (~14%).

Chromatin beads are classified using DNase-hypersensitity data and ChIP-seq data for H3K27ac. DNase-hypersensitive sites (DHS) are excellent markers to locate promoters and enhancers (and so TF-binding sites[19,54]), whereas H3K27ac modifications strongly correlate with open chromatin[19]. Therefore, if the 3 kbp region corresponding to a chromatin bead has a DHS, then that bead is a TU; if it has H3K27ac, it is a euchromatin bead, and all other beads are non-binding (heterochromatic). We call this the "DHS" model. As properties of different chromatin segments have been catalogued using "hidden-Markov models" (HMMs)

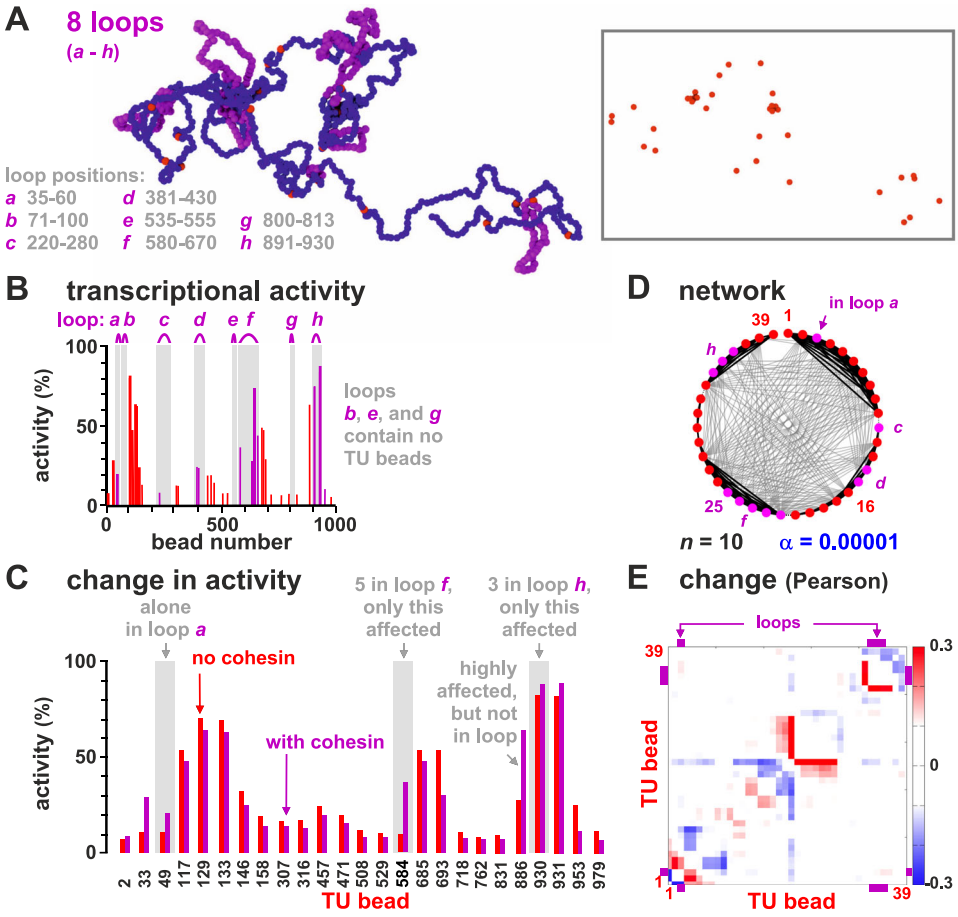

Fig. 5 Looping subtly affects transcriptional activity. Results of two sets of simulations are compared; one set as Fig. 1, in the other the chain contains eight permanent loops (to represent convergent loops stabilized by cohesin/CTCF). **A** Snapshot (beads within loops are magenta; TFs not shown; inset—same structure with only TUs shown). **B** Average transcriptional activity for each TU in the looped chain (magenta bars—values for TUs in loops; magenta arcs—loop positions). **C** Comparison between activity in wild type and looped configuration for the 25 TUs with significantly different values in the two sets ($p \simeq 0.003$; two-sided Student's *t*-test). **D** Regulatory network inferred from the matrix of Pearson correlations between expression levels of TUs (as Fig. 3A). **E** Change in Pearson correlation between TUs due to loops.

applied to many data sets[51], we alternatively classify beads according to HMM state; we call this the "HMM model" (Fig. S5). For more details, see Supplementary Note 3.

Simulations using the DHS model again yield clusters enriched in TUs and TFs (Fig. 7B). As before, aggregating data from many simulations allow determination of transcriptional activities of every bead, which we compare with those of corresponding regions determined experimentally[55] by GRO-seq (global run-on sequencing[56]); activities of all 3 kbp regions are ranked from high to low, binned into quintiles, and compared. In Fig. 7C, squares near the diagonal from bottom-left to top-right have high ranks (shown as red and yellow) compared to those off-diagonal (blue and purple) indicating good concordance between simulations and data. A specific sub-set of beads corresponding to SEs—which are highly active in vivo[57]—are also highly active in simulations (shown as white dots concentrated at top right). Plots showing the rank of transcriptional activities in simulations and experiments in selected genomic regions are shown in Fig. S6. Simulations yield patterns qualitatively closer to those obtained with GRO-seq than those given by poly(A)$^+$ RNA-seq, as the latter only include genic transcription. Concordance between results from simulations and GRO-seq is confirmed by the Spearman rank correlation (~0.38 for all beads; $p < 10^{-12}$; this measure is used because it is less sensitive to outliers; Fig. 7D). Restricting analysis just to TUs provides a more stringent comparison (as all TUs bind TFs with equal affinity); it still yields a significant correlation ($r \simeq 0.32$, $p < 10^{-12}$; Fig. 7D). As neighbouring high-affinity regions tend to have roughly similar transcriptional rates in both simulations and data, we also average rates found in active "patches" (contiguous sets of beads which are either all TUs or all labelled as euchromatin), but found this has no significant effect (Fig. 7D). Concordance was confirmed using our HMM model (Fig. 7D, right, and Fig. S5). Adding cohesin-mediated looping to simulations involving the DHS model did not significantly change agreement with experimental data (e.g., for TUs only, $r \simeq 0.33$, $p < 10^{-12}$). Similar agreement with GRO-seq data was obtained from simulations applied to the H1 human embryonic stem-cell line (for TUs using the DHS model, $r \simeq 0.29$, $p < 10^{-12}$), and to the GM12878 cell line (DHS model, $r \simeq 0.33$, $p < 10^{-12}$).

As in the chromosome fragment simulations (Fig. S1B), the transcriptional activity of a TU in our model anticorrelates with the distance to the nearest TU. In our HSA14 simulations, the presence of heterochromatin slightly reduces the absolute value of the correlation, which however remains highly significant (Spearman correlation $r \simeq -0.83$, $p < 10^{-12}$). Interestingly, the experimental GRO-seq signal of a DHS also anticorrelates with the distance to the nearest DHS in a significant way, although more weakly than in simulations (Fig. S7; over the whole genome the Spearman correlation is $r \sim -0.23$, $p < 10^{-12}$).

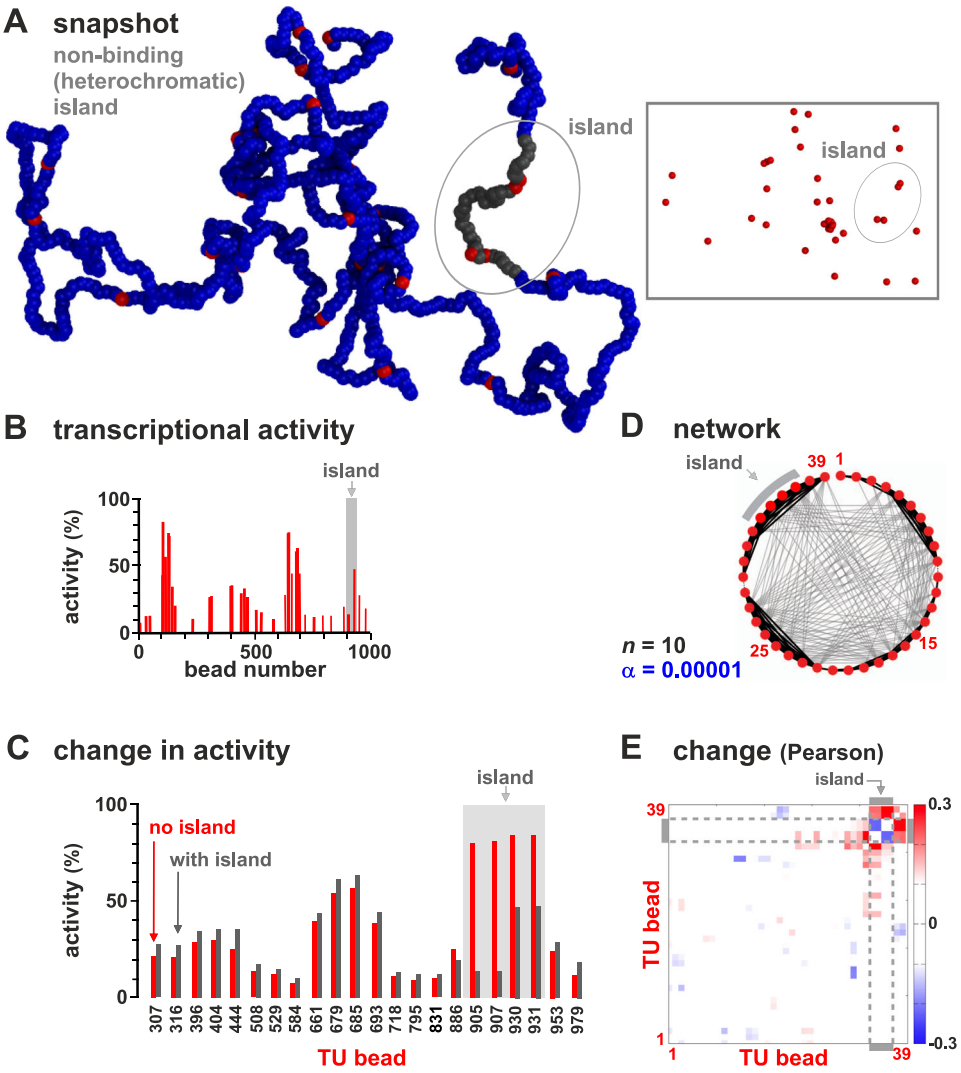

Fig. 6 Neighboring heterochromatin affects transcriptional activity. Results from two sets of simulations (at least 800 runs for each condition) are compared; one set as Fig. 1, in the other beads around TU beads 905, 907, 930, and 931 (from bead 901 to 940) are non-binding (to represent embedding the TU beads in heterochromatin). **A** Snapshot with heterochromatic beads shown in gray (TFs not shown; inset—the same structure with only TUs). **B** Average transcriptional activity for each TU. **C** Comparison of average transcriptional activity with respect to wild type for the 22 TUs with significantly different values in the two sets ($p \simeq 0.003$; two-sided Student's *t*-test). **D** Regulatory network inferred from the matrix of Pearson correlations between activities of TUs (as Fig. 3A). **E** Change in Pearson correlation between TUs due to heterochromatin.

Networks inferred from simulations are qualitatively similar to experimental ones. Regulatory networks emerging from our whole-chromosome simulations are again small-world and highly connected (Fig. S8 and Supplementary Note 4). To facilitate comparison with previous results, we select four segments of HSA14 that have the same length as the one considered in Fig. 3 (i.e., 3 Mbp), and roughly the same density of TUs; all four segments again have highly connected components (compare Fig. S8 and Fig. 3). However, patterns in real chromosomes and artificial fragments are quite different. In HSA14 networks, there are more positive interactions between sets of adjacent TUs and other sets that are >10 beads distant in sequence space (black lines across the middle of circles in Fig. S8).

Whole-chromosome networks also have the following statistical properties. First, their node-degree distribution decays exponentially (Fig. S9A)—as found in gene networks[58] but not in transcription factor interaction networks, which are often scale-free[59]. Second, they are modular (as clusters arising due to the bridging-induced attraction are the basic co-regulated building blocks)—again as found in gene[58] and eQTL[60] networks. [Modularity is apparent from the blocks visible in the correlation matrices, such as in Fig. S2.] Third, node degree broadly correlates with transcriptional activity (Spearman correlation 0.59, p value $< 10^{-12}$)—as in gene coregulation networks[58].

Contact maps found by simulations are qualitatively similar to Hi-C. We previously showed[16] that simulations involving two different TFs (binding to active and inactive regions, respectively) yield contact maps much like those found with Hi-C[42]. Therefore, we expected the present simulations to reflect Hi-C data poorly as they involve only one TF binding to the minor (i.e., active) fraction of the genome, so contacts made by this structured minority would be obscured by those due to the unstructured majority. Even so, simulations yield contact maps broadly similar to those obtained by Hi-C (Fig. 7E). To measure the agreement, we use a comparison based on contact maps restricted to TUs as anchors—which may be considered as equivalent to interactions obtained by promoter-capture HiC[61].

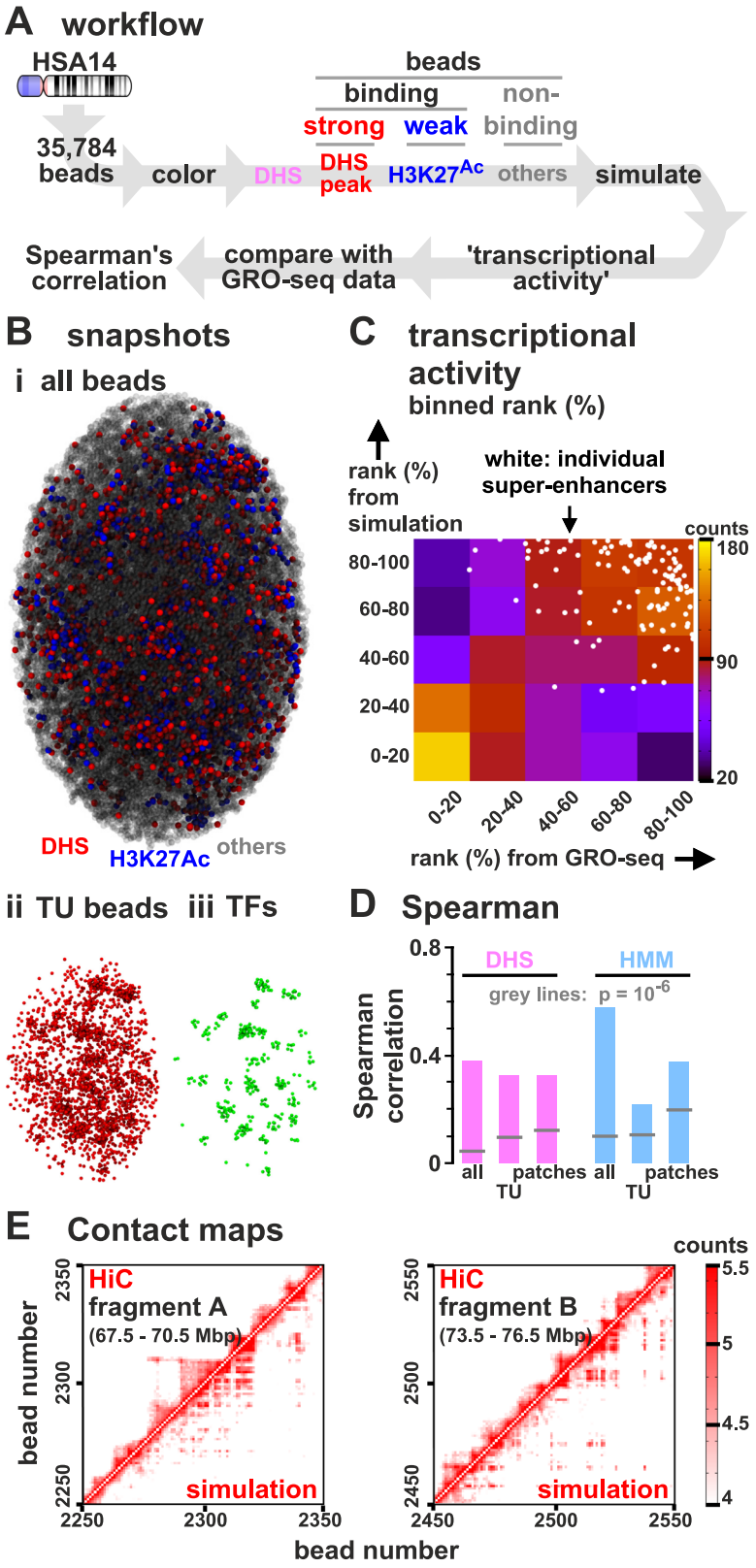

These yield good concordance (Fig. 7E; Pearson coefficient $r = 0.82$; $r = 0.47$ when monitoring only long-range contacts between TUs at least 300 kbp away, $p < 10^{-6}$ in both cases). The exponent with which contact probability decays with 1D distance is ~−1.1 in experiments, and ~−0.8 in simulations (fitted for 1D distances between ~30 kbp and 1.5 Mbp), both broadly consistent with the −1 value expected for a fractal globule[62]. The small discrepancy may point to our simulations slightly overestimating the weight of long-range contacts, perhaps because we do not include loop extrusion.

Overall the results obtained in our HSA14 simulations show that a simple model based on 3D chromatin organisation captures much of the complexity in 3D structure and transcription of a whole human chromosome.

Fig. 7 Comparison of transcriptional activities of TUs on HSA14 in HUVECs determined using simulations and GRO-seq. A Workflow (DHS model). Simulations (244 runs) involve a chain (35,784 beads) representing HSA14, and 1700 switchable TFs confined in an ellipsoidal territory. Beads are classified as TUs (red, strong binding), euchromatic (blue, weak binding), or heterochromatic (grey, non-binding). Transcriptional activities from simulations are compared with those of GRO-seq data, by measuring the Spearman rank correlation. **B** (i) Snapshot (TFs not shown). (ii, iii) TU beads and TFs in this configuration. **C** Comparison of transcriptional activities of TUs from simulations and GRO-seq (ranked from 0 to 100%, then binned in quintiles and showed as a heat map). A scatter plot of unbinned ranks of beads corresponding to SEs are superimposed (white circles). **D** Comparison of transcriptional activities from simulations (for both DHS and HMM models) and GRO-seq for all 3 kb regions/beads, only TUs, and only connected patches of binding beads (see text). All correlations are significant ($p < 10^{-6}$; two-sided Student's *t*-test, indicated by grey lines). **E** (i, ii) Capture-HiC-like contact maps obtained from simulations and experiments[42] showing logarithm of number of contacts between 30 kbp bins which contain TUs.

Modelling chromosome 22 carrying the diGeorge deletion. Our approach can, in principle, be applied to study any chromosome providing appropriate genomic data are available (e.g., on DNase hypersensitivity and histone acetylation). As a proof of principle, we studied the effect of deleting ~2.55 Mbp from HSA22—an alteration which is associated with the diGeorge syndrome (Fig. 8A) (https://dosage.clinicalgenome.org/clingen_region.cgi?id=ISCA-37446). This syndrome affects ~1 in 4000 people, and the variable symptoms include congenital heart problems, frequent infections, developmental delays, and learning problems.

We predict a multitude of small effects in TU activity, both near and far away from the deletion (see the Manhattan plot in Fig. 8Bi). In particular, most TUs are slightly up-regulated, as fewer TUs compete for the same number of factors, and the TUs which change the most have intermediate transcriptional activities in the wild type (Fig. S10). The *p* values associated with the change in transcriptional activities vary widely, and comparison of the observed distribution with the null hypothesis (indicating that changes in measured transcription are due to random variation) shows the observed is highly enriched in small *p* values (Fig. 8Bii), as is generally the case with results from GWAS[5,6]. The regulatory network is also re-wired (Fig. 8C). Results are consistent with measurements of differential gene expressions in patients, which showed both a large number of up-regulated and down-regulated genes[63]. A more quantitative comparison between experiments and simulations would benefit from having GRO-seq data that include non-genic transcription.

Clearly, this approach opens up a rich field of study. For instance, while there may be processes which occur in vivo which are not represented in our model, it could still give an indication of the genes most likely to be affected by any chromosome rearrangement.

Discussion

We have described a parsimonious 3D stochastic model for transcriptional dynamics based on multivalent binding of factors and polymerases (TFs) to genic and non-genic transcriptional units (TUs) in a chain representing a chromatin fibre. A distinctive feature of our framework is that it is fitting-free, which means the model is truly predictive and can provide a mechanistic understanding of the phenomena we observe. On the other hand, the absence of fitting renders it challenging to obtain a fully quantitative agreemeent between modelling and experiment.

In our simulations two types of fibres were considered: a 3 Mbp fragment with randomly-positioned TUs, which is useful to exemplify emerging trends, and human chromosomes 14 and 22 where TUs were appropriately positioned according to bioinformatic data. Despite deliberately excluding any explicit underlying network of biochemical regulation, our model nevertheless yields some notable results. These depend on having a low TF copy-number—a feature compatible with observations in vivo[23]. First, since TFs bind with the same affinity to all TUs, one might expect the latter to all be transcribed similarly, but they are not (Fig. 1). This is largely due to inter-TU spacing; TUs lying close together in 1D sequence space tend to be the most active (Fig. 1C) with positively correlated dynamics reminiscent of transcriptional bursting (Fig. 2B). This is because they often cluster into structures which are analogous to the phase-separated transcription hubs/factories seen experimentally[7,10], or to contact domains formed by accessible DNA sites found by high-resolution mapping of chromatin interactions by microC[30]. Second, switching off binding at any TU significantly affects the activity of many others, both near and far away in sequence space (Fig. 4). Third, introducing stable loops has subtle effects (Fig. 5), consistent with the result that cohesin knock-outs and degrons lead to small global changes in expression[49], although they can be important for inducible gene response in selected cases[46]. Fourth, transcriptional activity of a TU is strongly affected by the local environment in ways that are reminiscent of the silencing of a gene by incorporation into heterochromatin[52] (Fig. 6), or activation by embedment in euchromatin (Fig. S4). Fifth, the stochasticity seen in individual simulations reflects that detected by single-cell transcriptomics and single-cell Hi-C. Nevertheless, this variability does not prevent emergence of robust phenotypes in a cell population. Sixth, our simple fitting-free model predicts patterns of transcriptional activity in human chromosomes that promisingly and significantly correlate with experimental GRO-seq data (Fig. 7). This suggests that chromatin structure significantly constrains transcriptional activity. We hypothesise that additional downstream biochemical regulation, not included in our model, may provide a tool to adjust this underlying "structural" pattern of activity in a way which may be required for appropriate biological function.

Finally, our results enable us to reconcile two conflicting sets of data, namely that regulatory networks are both complex (as GWAS shows that thousands of loci around the genome control complex phenotypes[5,6]) and simple (as over-expressing just four Yamanaka factors switches cell fate[4]). Thus, our simulations reveal complex small-world networks of mutual up- and down-regulation (Figs. 3 and S8), consistent with GWAS results. However, increasing TF copy-number dramatically simplifies network structure (Fig. 3). We suggest such a simplification occurs when a fibroblast is reprogrammed into a pluripotent stem cell by over-expressing the Yamanaka factors; the high factor concentration simplifies the network so that the factors can combine to switch the phenotype (Fig. S11).

Taken together, these results suggest the activity—or inactivity—of every genomic region affects that of every other region to some extent. We describe our framework as "pan-genomic" (Fig. S11). This is reminiscent of the omnigenic model[5,6] in the sense that many loci are involved, all having small effects. However, it differs as it provides an underlying mechanism for pangenomic effects, by positing a direct and immediate effect of structure on regulation at the transcriptional level, which contrasts with the non-trivial post-transcriptional pathways envisioned by the omnigenic model. Additionally, our pangenomic model yields a natural framework to qualitatively understand mutually exclusive gene expression, when switching on one gene in a family turns off all others (as in

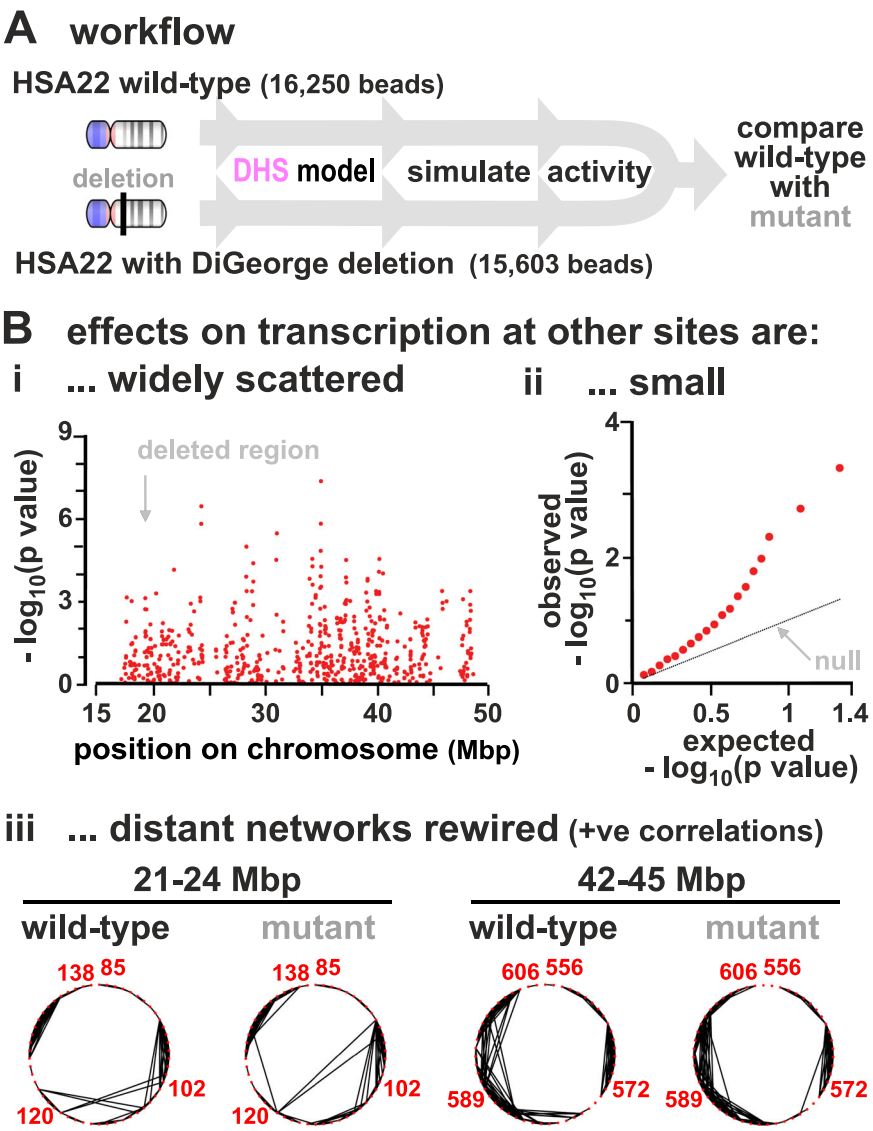

Fig. 8 Modelling effects of the DiGeorge deletion in HSA22. A Workflow. Simulations (800 simulations/condition) for wild type (17,102 beads) and deletion (16,250 beads, where wild-type beads 6305–7156 are cut, corresponding to a deletion of chr22:18,912,231–21,465,672 in hg19). [Agreement between predicted transcriptional activity and GRO-seq in HSA22 is similar to that found for HSA14 (here, Spearman correlation is $r \sim 0.29$, $p < 10^{-6}$; two-sided Student's *t*-test).] **B** (i) Manhattan plot showing $-\log_{10}(p \text{ value})$ as a function of genomic position along HSA22 (position given in Mbp), for changes in TU transcriptional activities between wild type and deletion. (ii) Quantile–quantile plot showing expected versus observed values for $-\log_{10}(p \text{ value})$ for the same data in (i). Expected values are computed from the normal distribution (these correspond to the null hypothesis according to which the change in transcriptional activities in the deletion is purely due to random variation). (iii) Regulatory networks of two 3 Mbp segments in chromosome 22 inferred from the Pearson correlation matrix. Edges show positive correlations >0.12 ($p = 0.0007$). Segments chosen have roughly the same number of nodes in 3 Mbp as the short fragment (Fig. 3Aii).

developing olfactory neurons[64]). The current model to explain this phenomenon postulates a coupling between *cis*-acting up-regulation and *trans*-acting down-regulation. The pangenomic networks we find provide exactly this type of regulatory interactions (Fig. 3). Our results are also consistent with recent experiments and mathematical models showing that subtle changes in 3D structure can lead to large changes in transcription[65,66]. On the other hand, it is challenging within our current model to account for local negative feedback mechanisms leading to noise reduction or oscillations[11], as these are more likely to arise biochemically (an example is the p53–Mdm2 system which achieves stabilisation of the cellular concentration of p53 via a negative feedback loop[67]).

In conclusion, we have developed a framework that can be applied to predict the transcriptional activity of any genomic fragment in health or disease (Figs. 7 and 8) providing appropriate experimental data are available. Predictive power can be enhanced by incorporating additional TFs, and more suitable datasets of histone marks. Other features that can improve correlations between experiments and simulations are a more accurate modelling of cohesin loop formation by loop extrusion, and of the heteromorphic nature of chromatin[19]. We hope to report on work incorporating the latter two features in the future.

Methods

Polymer modelling. We model chromatin fibres and chromosomes as bead-and-spring polymers. A fibre has M monomers, each of size σ (corresponding to 3 kbp, or 30 nm[24]), and $\mathbf{r}_i$ denotes the position of the ith monomer in 3D space. Multivalent transcription factors (either active or inactive) are modelled as spheres, again with size σ for simplicity. There are n multivalent factors in a simulation (where n is varied systematically, see text and "Results" section for details), and N high-affinity binding sites, which we refer to as TU (or TU beads).

Any two monomers (i and j) in the chromatin fibre interact purely repulsively, via a Weeks–Chandler–Anderson potential, given by

$$U^{ij}_{\mathrm{WCA}} = 4k_{\mathrm{B}}T\left[\left(\frac{\sigma}{r_{ij}}\right)^{12} - \left(\frac{\sigma}{r_{ij}}\right)^{6} + \frac{1}{4}\right] \quad (1)$$

if $r_{ij} < 2^{1/6}\sigma$ and 0 otherwise, where r_{ij} is the separation of beads i and j. There is also a finite extensible non-linear elastic (FENE) spring acting between consecutive beads in the chain to enforce chain connectivity. This is given by

$$U^{ij}_{\mathrm{FENE}} = -\frac{K_{\mathrm{f}}R_0^2}{2}\ln\left[1 - \left(\frac{r_{ij}}{R_0}\right)^2\right] \quad (2)$$

where i and j are neighbouring beads, $R_0 = 1.6\sigma$ is the maximum separation between the beads, and $K_{\mathrm{f}} = 30k_{\mathrm{B}}T/\sigma^2$ is the spring constant. With simulations including permanent cohesin loops (Fig. 7 in the main text, and Supplementary Fig. S4), neighbouring monomers and monomers forming loops interact via harmonic, rather than FENE springs,

$$U^{ij}_{\mathrm{harmonic}} = K_{\mathrm{h}}\left(r_{ij} - \bar{R}\right)^2 \quad (3)$$

where i and j are neighbouring beads, $K_{\mathrm{h}} = 100k_{\mathrm{B}}T/\sigma^2$ is the harmonic spring constant, and $\bar{R}$ is the equilibrium spring distance. For these simulations, we use $\bar{R} = 1.1\sigma$ for bonds joining neighbouring monomers along the chain, and $\bar{R} = 1.8\sigma$ for bonds joining loop-forming monomers. The harmonic potential is used instead of the FENE one to enhance numerical stability.

Finally, a triplet of neighbouring beads interact via a Kartky–Porod term to model the stiffness of the chromatin fibre. This term explicitly reads as follows:

$$U^{ij}_{\mathrm{KP}} = \frac{k_{\mathrm{B}}T\ell_{\mathrm{p}}}{\sigma}\left[1 - \frac{\vec{t}_i \cdot \vec{t}_j}{|\vec{t}_i||\vec{t}_j|}\right] \quad (4)$$

where i and j are neighbouring beads, $\vec{t}_i$ is the tangent vector connecting beads i to $i+1$, and ℓ_{p} is related to the persistent length of the chain: this parameter is set to 3σ in our simulation, which corresponds to a relatively flexible fibre—the resulting persistence length is within the range of values estimated for chromatin from experiments and computer simulations[68].

The interaction between a chromatin bead, a, and a multivalent TF, b, is modeled through a truncated and shifted Lennard–Jones potential, given by

$$U^{ab}_{\mathrm{LJ}} = 4\epsilon_{ab}\left[\left(\frac{\sigma}{d_{ab}}\right)^{12} - \left(\frac{\sigma}{d_{ab}}\right)^{6} - \left(\frac{\sigma}{r_c}\right)^{12} + \left(\frac{\sigma}{r_c}\right)^{6}\right], \quad (5)$$

for d_{ab} (the distance between the centres of chromatin bead and protein) smaller than r_c, and 0 otherwise. The parameter r_c is the interaction cut-off; it is set to $r_c = 2^{1/6}\sigma$ for inactive proteins or for active proteins and non-binding chromatin beads (this cutoff results in a Weeks–Chandler–Anderson potential and purely repulsive interactions), or to $r_c = 1.8\sigma$ for an active protein and a binding chromatin bead (this results in an attractive interaction). In all cases, the potential is shifted to zero at the cut-off in order to have a smooth potential. Purely repulsive interactions are modeled by setting $\epsilon_{ab} = k_{\mathrm{B}}T$, while attractive interactions are modeled using $\epsilon_{ab} = 3k_{\mathrm{B}}T$ for active TF and low-affinity beads, and to $\epsilon_{ab} = 8k_{\mathrm{B}}T$ for active TF and high-affinity (TU) beads.

A TU bead (or more generally any chromatin bead in Fig. 8D in the main text) is said to be transcribed if it is bound to a factor—i.e., if there is at least a TF whose centre lies within a range $r_c = 1.8\sigma$ away from the bead centre.

The time evolution of each bead in the simulation (whether TF or chromatin bead) is governed by the following Langevin equation:

$$m_i\frac{d^2\vec{r}_i}{dt^2} = -\nabla U_i - \gamma_i\frac{d\vec{r}_i}{d}t + \sqrt{2k_{\mathrm{B}}T\gamma_i}\vec{\eta}_i(t), \quad (6)$$

where U_i is the total potential experienced by bead i, $m_i \equiv m$ and $\gamma_i \equiv \gamma$ are its mass and friction coefficient (equal for all beads in our simulations), and $\vec{\eta}_i$ is a stochastic noise vector with the following mean and variance:

$$\langle\vec{\eta}(t)\rangle = 0; \quad \langle\eta_{i,\alpha}(t)\eta_{j,\beta}(t')\rangle = \delta_{ij}\delta_{\alpha\beta}\delta(t-t'), \quad (7)$$

where the Latin and Greek indices run over particles and Cartesian components, respectively, and δ denotes here the Kronecker delta.

As is customary[69], we set $m/\xi = \tau_{\mathrm{LJ}} = \tau_{\mathrm{B}}$, with the LJ time $\tau_{\mathrm{LJ}} = \sigma\sqrt{m/\epsilon}$ and the Brownian time $\tau_{\mathrm{B}} = \sigma^2/D$, where ϵ is the simulation energy unit, equal to $k_{\mathrm{B}}T$, and $D = k_{\mathrm{B}}T/\gamma$ is the diffusion coefficient of a bead of size σ. From the Stokes friction coefficient for spherical beads of diameter σ we have that $\xi = 3\pi\eta_{\mathrm{sol}}\sigma$ where η_{sol} is the solution viscosity. One can map this to physical units by setting $T = 300$ K and $\sigma = 30$ nm, as above, and by setting the viscosity to the effective viscosity of the nucleoplasm, which is scale-dependent and ranges between 10 and100 cP for objects of the size of our chromatin bead[70]. This leads to $\tau_{\mathrm{LJ}} = \tau_{\mathrm{B}} = 3\pi\eta_{\mathrm{sol}}\sigma^3/\epsilon \simeq 0.6$–6 ms. The Brownian time τ_{B} is our unit of time in simulations. The numerical integration of Eq. (6) is performed using a standard velocity-Verlet algorithm with time step $\Delta t = 0.01\tau_{\mathrm{B}}$ and is implemented in the LAMMPS engine[71]. Protein switching is including by stochastically changing the type of TF beads every 10,000 timesteps (equivalently, every 100 Brownian times), with probabilities such that the switching off rate is of $\alpha = 10^{-5}\tau_{\mathrm{B}}^{-1}$, or 0.017–0.17 s^{-1}. In simulations of the toy model (Figs. 1–7 in the main text and Suppl. Figs. S1–S4), the switching on rate is equal to α; in chromosome 14/22 simulations (Fig. 8 in the main text and Suppl. Fig. S5), it is equal to $\alpha/4$. Consequently, in steady state the average number of active and inactive proteins is equal in simulations of the toy model, whereas the average number of inactive proteins is fourfold larger than that of active proteins in chromosome 14/22 simulations.

For more details on simulations, see Supplementary Notes 1 and 3.

Reporting summary. Further information on research design is available in the Nature Research Reporting Summary linked to this article.

Data availability

The datasets generated during and/or analysed during the current study have been deposited in Edinburgh DataShare [https://doi.org/10.7488/ds/3110]. To compare the predicted transcriptional activity of chromosome 14 outputted by our simulations with experiments, we use GRO-seq data. For HUVECs, we use the datasets GEO: GSM2486801, GSM2486802, GSM2486803. For hESCs, we use GEO: GSM1579367, GSM1579368. Super-enhancer regions considered here are those identified in ref. [57], and available in the dbSUPER database [http://asntech.org/dbsuper/].

Code availability

The code used for the simulation is LAMMPS, which is publicly available at https://lammps.sandia.gov/. Custom codes written to analyse data are available from the corresponding author upon request, or they can be downloaded from https://git.ecdf.ed.ac.uk/dmarendu/omnigenomic-model (access can be requested from the corresponding author).

Received: 27 May 2021; Accepted: 30 August 2021;
Published online: 01 October 2021

References

1. Alberts, B., Johnson, A., Lewis, J., Morgan, D. & Raff, M. *Molecular Biology of the Cell* (Taylor & Francis, 2014).
2. Davis, R. L., Weintraub, H. & Lassar, A. B. Expression of a single transfected cDNA converts fibroblasts to myoblasts. *Cell* **51**, 987–1000 (1987).
3. Dall'Agnese, A. et al. Transcription factor-directed re-wiring of chromatin architecture for somatic cell nuclear reprogramming toward trans-differentiation. *Mol. Cell* **76**, 453–472 (2019).
4. Takahashi, K. et al. Induction of pluripotent stem cells from adult human fibroblasts by defined factors. *Cell* **131**, 861–872 (2007).
5. Boyle, E. A., Li, Y. I. & Pritchard, J. K. An expanded view of complex traits: from polygenic to omnigenic. *Cell* **169**, 1177–1186 (2017).
6. Liu, X., Li, Y. I. & Pritchard, J. K. Trans effects on gene expression can drive omnigenic inheritance. *Cell* **177**, 1022–1034 (2019).
7. Cook, P. R. & Marenduzzo, D. Transcription-driven genome organization: a model for chromosome structure and the regulation of gene expression tested through simulations. *Nucleic Acids Res.* **46**, 9895–9906 (2018).
8. Andersson, R. et al. An atlas of active enhancers across human cell types and tissues. *Nature* **507**, 455–461 (2014).
9. Javierre, B. M. et al. Lineage-specific genome architecture links enhancers and non-coding disease variants to target gene promoters. *Cell* **167**, 1369–1384 (2016).
10. Cramer, P. Organization and regulation of gene transcription. *Nature* **573**, 45–54 (2019).
11. Sneppen, K., Krishna, S. & Semsey, S. Simplified models of biological networks. *Annu. Rev. Biophys.* **39**, 43–59 (2010).
12. Smolen, P., Baxter, D. A. & Byrne, J. H. Modeling transcriptional control in gene networks—methods, recent results, and future directions. *Bull. Math. Biol.* **62**, 247–292 (2000).
13. Pombo, A. & Dillon, N. Three-dimensional genome architecture: players and mechanisms. *Nat. Rev. Mol. Cell Biol.* **16**, 245–257 (2015).
14. Spielmann, M., Lupiáñez, D. G. & Mundlos, S. Structural variation in the 3D genome. *Nat. Rev. Genet.* **19**, 453–467 (2018).
15. Barbieri, M. et al. Complexity of chromatin folding is captured by the strings and binders switch model. *Proc. Natl Acad. Sci. USA* **109**, 16173–16178 (2012).
16. Brackley, C. A., Johnson, J., Kelly, S., Cook, P. R. & Marenduzzo, D. Simulated binding of transcription factors to active and inactive regions folds human chromosomes into loops, rosettes and topological domains. *Nucleic Acids Res.* **44**, 3503–3512 (2016).

17. Gilbert, N. & Marenduzzo, D. Genome organization: experiments and modeling. *Chromosome Res.* **25**, 1 (2017).
18. Pereira, M. C. F. et al. Complementary chromosome folding by transcription factors and cohesin. Preprint at *bioRxiv* https://doi.org/10.1101/305359 (2018).
19. Buckle, A., Brackley, C. A., Boyle, S., Marenduzzo, D. & Gilbert, N. Polymer simulations of heteromorphic chromatin predict the 3D folding of complex genomic loci. *Mol. Cell* **72**, 786–797 (2018).
20. Finn, E. H. et al. Extensive heterogeneity and intrinsic variation in spatial genome organization. *Cell* **176**, 1502–1515 (2019).
21. Brackley, C. A. et al. Ephemeral protein binding to DNA shapes stable nuclear bodies and chromatin domains. *Biophys. J.* **28**, 1085–1093 (2017).
22. Steurer, B. et al. Live-cell analysis of endogenous GFP-RPB1 uncovers rapid turnover of initiating and promoter-paused RNA polymerase II. *Proc. Natl Acad. Sci. USA* **115**, E4368–E4376 (2018).
23. Brewster, R. C. et al. The transcription factor titration effect dictates level of gene expression. *Cell* **156**, 1312–1323 (2014).
24. Brackley, C. A., Taylor, S., Papantonis, A., Cook, P. R. & Marenduzzo, D. Nonspecific bridging-induced attraction drives clustering of DNA-binding proteins and genome organization. *Proc. Natl Acad. Sci. USA* **110**, E3605–E3611 (2013).
25. Brackley, C. Polymer compaction and bridging-induced clustering of protein-inspired patchy particles. *J. Phys. Condens. Matter* **32**, 314002 (2020).
26. Kilic, S., Bachmann, A. L., Bryan, L. C. & Fierz, B. Multivalency governs HP1α association dynamics with the silent chromatin state. *Nat. Commun.* **6**, 7313 (2015).
27. Cook, P. R. The organization of replication and transcription. *Science* **284**, 1790–1795 (1999).
28. Papantonis, A. et al. TNFα signals through specialized factories where responsive coding and miRNA genes are transcribed. *EMBO J.* **31**, 4404–4414 (2012).
29. Shrinivas, K. et al. Enhancer features that drive formation of transcriptional condensates. *Mol. Cell* **75**, 549–561 (2019).
30. Hsieh, T.-H. S. et al. Resolving the 3D landscape of transcription-linked mammalian chromatin folding. *Mol. Cell* **78**, 539–553 (2020).
31. Ryu, J.-K. et al. Bridging-induced phase separation induced by cohesin SMC protein complexes. *Sci. Adv.* **7**, eabe5905 (2021).
32. Pombo, A. et al. Regional specialization in human nuclei: visualization of discrete sites of transcription by RNA polymerase III. *EMBO J.* **18**, 2241–2253 (1999).
33. Faro-Trindade, I. & Cook, P. R. A conserved organization of transcription during embryonic stem cell differentiation and in cells with high C value. *Mol. Biol. Cell* **17**, 2910–2920 (2006).
34. Beagrie, R. A. et al. Complex multi-enhancer contacts captured by genome architecture mapping. *Nature* **543**, 519–524 (2017).
35. Nagano, T. et al. Single-cell Hi-C reveals cell-to-cell variability in chromosome structure. *Nature* **502**, 59 (2013).
36. Macaulay, I. C. & Voet, T. Single cell genomics: advances and future perspectives. *PLoS Genet.* **10**, e1004126 (2014).
37. Muerdter, F. & Stark, A. Gene regulation: activation through space. *Curr. Biol.* **26**, R895–R898 (2016).
38. Fukaya, T., Lim, B. & Levine, M. Enhancer control of transcriptional bursting. *Cell* **166**, 358–368 (2016).
39. Bartman, C. R., Hsu, S. C., Hsiung, C. C.-S., Raj, A. & Blobel, G. A. Enhancer regulation of transcriptional bursting parameters revealed by forced chromatin looping. *Mol. Cell* **62**, 237–247 (2016).
40. Suter, D. M. et al. Mammalian genes are transcribed with widely different bursting kinetics. *Science* **332**, 472–474 (2011).
41. Humphries, M. D. & Gurney, K. Network 'small-world-ness': a quantitative method for determining canonical network equivalence. *PLoS ONE* **3**, e0002051 (2008).
42. Rao, S. S. et al. A 3d map of the human genome at kilobase resolution reveals principles of chromatin looping. *Cell* **159**, 1665 – 1680 (2014).
43. Fudenberg, G. et al. Formation of chromosomal domains by loop extrusion. *Cell Rep.* **15**, 2038–2049 (2016).
44. Brackley, C. A. et al. Non-equilibrium chromosome looping via molecular slip-links. *Phys. Rev. Lett.* **119**, 138101 (2017).
45. Oti, M., Falck, J., Huynen, M. A. & Zhou, H. Ctcf-mediated chromatin loops enclose inducible gene regulatory domains. *BMC Genomics* **17**, 252 (2016).
46. Cuartero, S. et al. Control of inducible gene expression links cohesin to hematopoietic progenitor self-renewal and differentiation. *Nat. Immunol.* **19**, 932–941 (2018).
47. Sasca, D. et al. Cohesin-dependent regulation of gene expression during differentiation is lost in cohesin-mutated myeloid malignancies. *Blood* **134**, 2195–2208 (2019).
48. Robson, M. I., Ringel, A. R. & Mundlos, S. Regulatory landscaping: how enhancer-promoter communication is sculpted in 3d. *Mol. Cell* **74**, 1110–1122 (2019).
49. Rao, S. S. et al. Cohesin loss eliminates all loop domains. *Cell* **171**, 305–320 (2017).
50. Gilbert, N. et al. Chromatin architecture of the human genome: gene-rich domains are enriched in open chromatin fibers. *Cell* **118**, 555–566 (2004).
51. Ernst, J. et al. Mapping and analysis of chromatin state dynamics in nine human cell types. *Nature* **473**, 43 (2011).
52. Timms, R. T., Tchasovnikarova, I. A. & Lehner, P. J. Position-effect variegation revisited: hushing up heterochromatin in human cells. *BioEssays* **38**, 333–343 (2016).
53. Wang, Y., Nagarajan, M., Uhler, C. & Shivashankar, G. Orientation and repositioning of chromosomes correlate with cell geometry-dependent gene expression. *Mol. Biol. Cell* **28**, 1997–2009 (2017).
54. Consortium, E. P. An integrated encyclopedia of dna elements in the human genome. *Nature* **489**, 57–74 (2012).
55. Niskanen, H. et al. Endothelial cell differentiation is encompassed by changes in long range interactions between inactive chromatin regions. *Nucleic Acids Res.* **46**, 1724–1740 (2017).
56. Jordán-Pla, A., Pérez-Martínez, M. E. & Pérez-Ortín, J. E. Measuring RNA polymerase activity genome-wide with high-resolution run-on-based methods. *Methods* **159**, 177–182 (2019).
57. Khan, A. & Zhang, X. dbsuper: a database of super-enhancers in mouse and human genome. *Nucleic Acids Res.* **44**, D164–D171 (2015).
58. Belcastro, V. et al. Transcriptional gene network inference from a massive dataset elucidates transcriptome organization and gene function. *Nucleic Acids Res.* **39**, 8677–8688 (2011).
59. Ouma, W. Z., Pogacar, K. & Grotewold, E. Topological and statistical analyses of gene regulatory networks reveal unifying yet quantitatively different emergent properties. *PLoS Comput. Biol.* **14**, e1006098 (2018).
60. Fagny, M. et al. Exploring regulation in tissues with eQTL networks. *Proc. Natl Acad. Sci. USA* **114**, E7841–E7850 (2017).
61. Mifsud, B. et al. Mapping long-range promoter contacts in human cells with high-resolution capture Hi-C. *Nat. Genet.* **47**, 598 (2015).
62. Mirny, L. A. The fractal globule as a model of chromatin architecture in the cell. *Chromosome Res.* **19**, 37–51 (2011).
63. Jalbrzikowski, M. et al. Transcriptome profiling of peripheral blood in 22q11. 2 deletion syndrome reveals functional pathways related to psychosis and autism spectrum disorder. *PLoS ONE* **10**, e0132542 (2015).
64. Alsing, A. K. & Sneppen, K. Differentiation of developing olfactory neurons analysed in terms of coupled epigenetic landscapes. *Nucleic Acids Res.* **41**, 4755–4764 (2013).
65. Xiao, J. Y., Hafner, A. & Boettiger, A. N. How subtle changes in 3D structure can create large changes in transcription. *eLife* **10**, e64320 (2021).
66. Zuin, J. et al. Nonlinear control of transcription through enhancer-promoter interactions. Preprint at *bioRxiv* https://doi.org/10.1101/2021.04.22.440891 (2021).
67. Harris, S. L. & Levine, A. J. The p53 pathway: positive and negative feedback loops. *Oncogene* **24**, 2899–2908 (2005).
68. Dekker, J., Rippe, K., Dekker, M. & Kleckner, N. Capturing chromosome conformation. *Science* **295**, 1306–1311 (2002).
69. Kremer, K. & Grest, G. S. Dynamics of entangled linear polymer melts: a molecular-dynamics simulation. *J. Chem. Phys.* **92**, 5057–5086 (1990).
70. Michieletto, D., Orlandini, E. & Marenduzzo, D. Polymer model with epigenetic recoloring reveals a pathway for the de novo establishment and 3D organization of chromatin domains. *Phys. Rev. X* **6**, 041047 (2016).
71. Plimpton, S. Fast parallel algorithms for short-range molecular dynamics. *J. Comp. Phys.* **117**, 1–19 (1995).

Acknowledgements

We thank the European Research Council (ERC CoG 648050 THREEDCELLPHYSICS) for support.

Author contributions

C.A.B., N.G., D. Michieletto, A.P., P.R.C., M.C.F.P., and D. Marenduzzo designed research; C.A.B., M.C.F.P., and D. Marenduzzo performed research; C.A.B., N.G., D. Michieletto, A.P., M.C.F.P., P.R.C., and D. Marenduzzo analysed the data and wrote the manuscript.

Competing interests

The authors declare no competing interests.

Additional information

Supplementary information The online version contains supplementary material available at https://doi.org/10.1038/s41467-021-25875-y.

Correspondence and requests for materials should be addressed to D. Marenduzzo.

Peer review information *Nature Communications* thanks the anonymous reviewers for their contribution to the peer review of this work. Peer reviewer reports are available.

Reprints and permission information is available at http://www.nature.com/reprints

Publisher's note Springer Nature remains neutral with regard to jurisdictional claims in published maps and institutional affiliations.

Open Access This article is licensed under a Creative Commons Attribution 4.0 International License, which permits use, sharing, adaptation, distribution and reproduction in any medium or format, as long as you give appropriate credit to the original author(s) and the source, provide a link to the Creative Commons license, and indicate if changes were made. The images or other third party material in this article are included in the article's Creative Commons license, unless indicated otherwise in a credit line to the material. If material is not included in the article's Creative Commons license and your intended use is not permitted by statutory regulation or exceeds the permitted use, you will need to obtain permission directly from the copyright holder. To view a copy of this license, visit http://creativecommons.org/licenses/by/4.0/.

© The Author(s) 2021

Complex small-world regulatory networks emerge from the 3D organisation of the human genome: Supplementary Information

C. A. Brackley *et al.*

Supplementary Figures

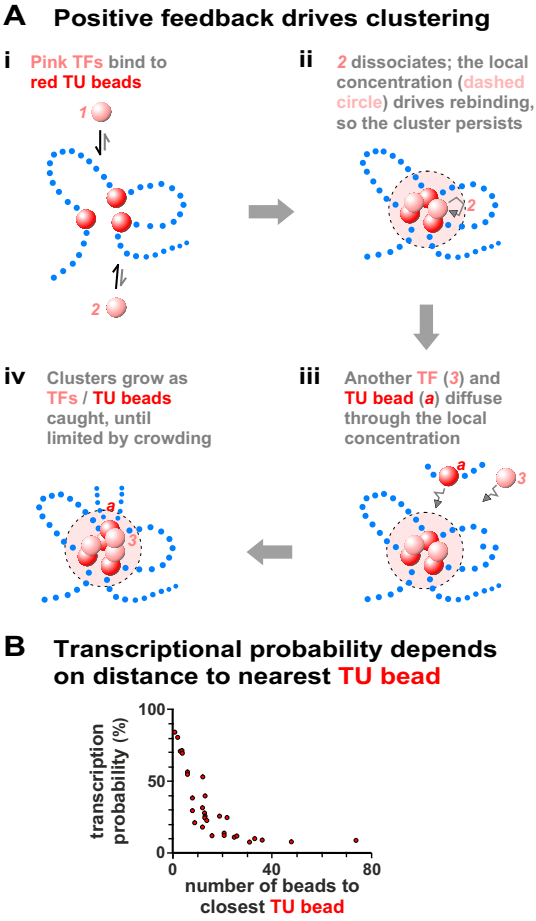

Supplementary Figure 1: **Clusters form spontaneously, and nearby TU beads tend to be transcribed more often. A.** Clustering is driven by positive feedback (the "bridging-induced attraction") [1, 2]. (i) Multivalent TFs *1* and *2* (pink) bind reversibly to red TU beads; each blue dot represents many non-binding beads. No other attractive forces between TFs or between TUs are specified. (ii) The two TFs bound; each stabilizes a loop. The local concentration of red TUs in the dashed volume has now increased, so if pink TF *2* dissociates it is likely to rebind to the same cluster (grey arrow); therefore, the cluster is likely to persist. (iii) The high local concentration also drives cluster growth. Here, the cluster will catch red TU *a* and pink TF *3*, as they diffuse through this local region. (iv) Cluster growth continues due to this positive feedback until limited by the entropic costs of crowding together ever more loops. **B.** Scatter plot where each point represents a TU bead, and the horizontal axis gives the distance along the chain in beads to the nearest neighbouring TU. A strong anticorrelation with transcriptional activity is evident. The positive feedback described in (A) ensures that the closer a TU is to another TU, the higher the probability it will cluster and be transcriptionally active.

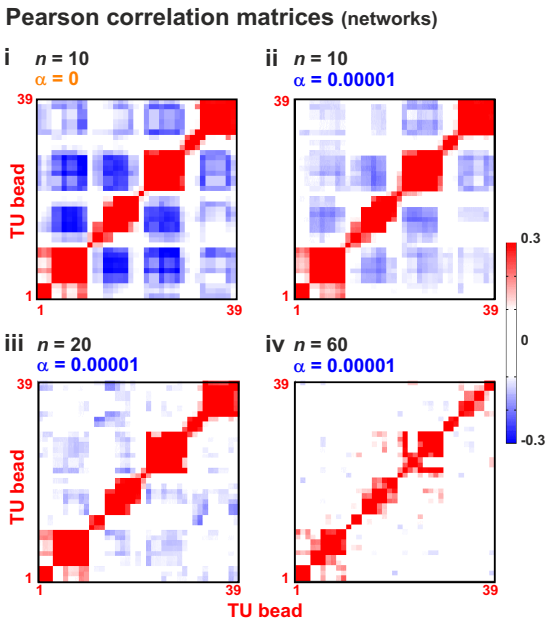

Supplementary Figure 2: **Pearson correlation matrices.** Pearson correlation (covariance) matrices for simulations in Fig. 3 in the main text. These are used to construct regulatory networks.

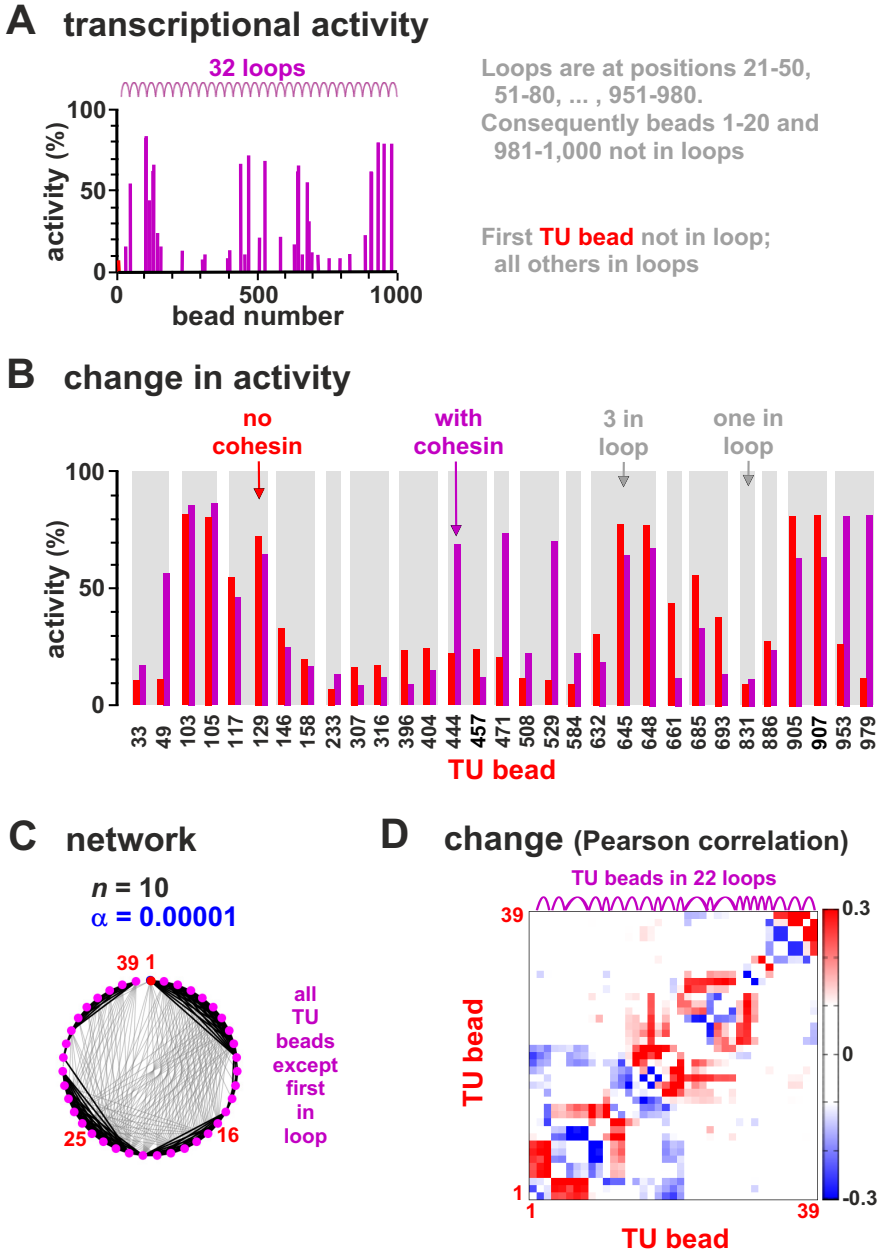

Supplementary Figure 3: **Transcriptional activity in a chain with closely-packed loops.** Results of two sets of simulations ($\geq$ 800 simulations/condition) are compared; one set as Fig. 1 in the main text, in the other the chain contains 32 consecutive and closely-packed permanent loops of size 30 σ. **A.** Average transcriptional activity for each TU in the looped set (magenta bars indicate values for TUs in loops, and magenta arcs loop positions). **B.** Comparison between expression in wild-type and looped configuration for 31 TUs with significantly different values in the two sets ($p \simeq 0.003$; Students t-test). **C.** Regulatory network inferred from the matrix of Pearson correlations between expression of TUs (as Fig. 3A in the main text). **D.** Change in Pearson correlation between TUs due to introduction of loops.

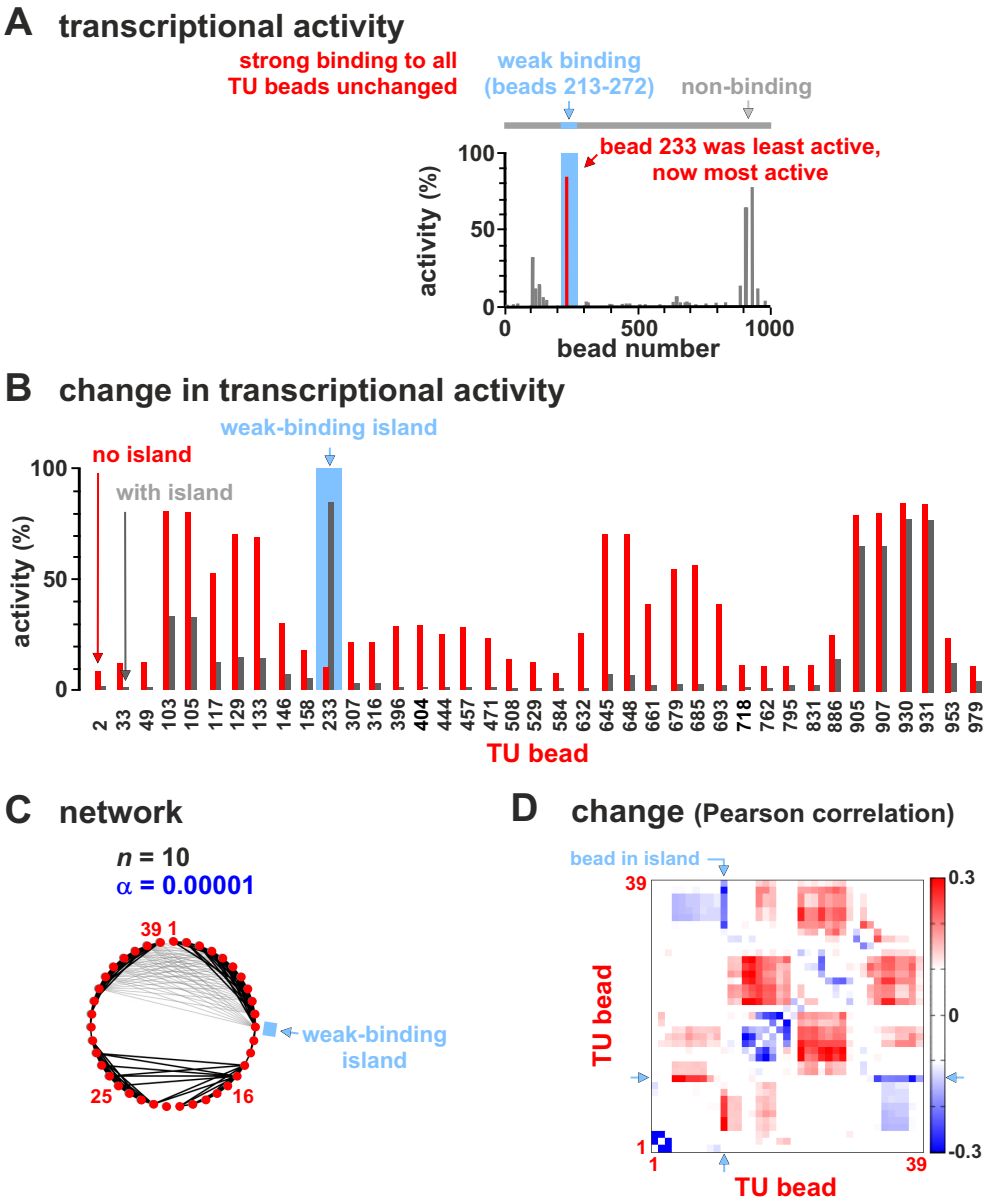

Supplementary Figure 4: **Transcriptional activity in a heterochromatic chain with an euchromatic island.** Results from two sets of simulations (800 simulations/condition) are compared; one set as Fig. 1 in the main text, in the other all non-TU beads are heterochromatic apart from those between bead 213 and 272 inclusive (to represent a euchromatic island). **A.** Average transcriptional activity for each TU bead. Grey bars: values for TUs in heterochromatin. **B.** Comparison of average transcriptional activity with respect to the wild-type for all 39 TUs; these all have significantly-different values in the two sets ($p \simeq 0.003$; Students t-test). **C.** Regulatory network inferred from the matrix of Pearson correlations between transcriptional activities of TUs (as Fig. 3A in the main text). **D.** Change in Pearson correlation between TUs with respect to the wild-type.

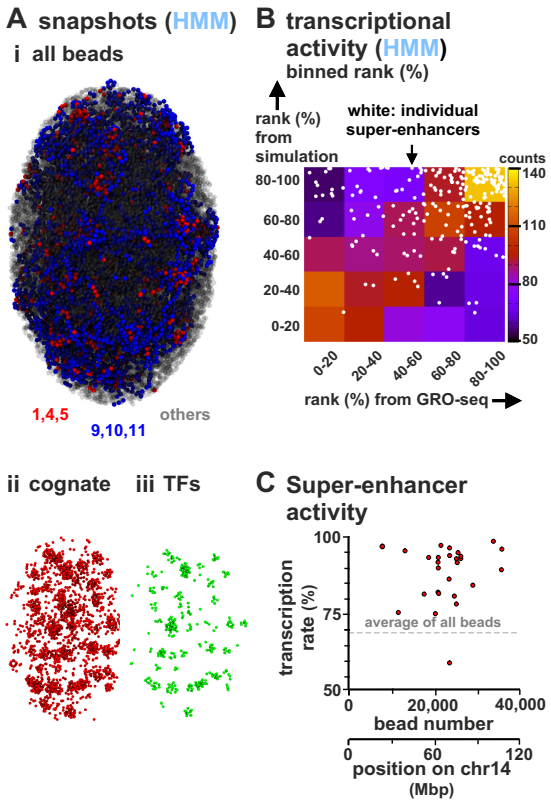

Supplementary Figure 5: **Comparison of transcriptional activities of human chromosome** 14 **in HUVECs determined using simulations (HMM model) and GRO-seq. A. Snapshot.** (i) All beads on the chain (TFs not shown, numbers refer to state numbers in HMM tracks in [3] used to color beads). (ii, iii) TU beads and TFs corresponding to the configuration in (i). **B.** Comparison of transcriptional activities of red TUs in simulations and GRO-seq (ranked from 0−100% and binned in quintiles). A scatter plot of unbinned ranks of beads corresponding to SEs are superimposed (white circles). **C.** Transcription rate of SEs. For a given SE, the rate is the average of all TUs in the SE region. We find 26 of 27 SEs have a higher-than-average expression/transcriptional activity. Data correspond to 100 simulations.

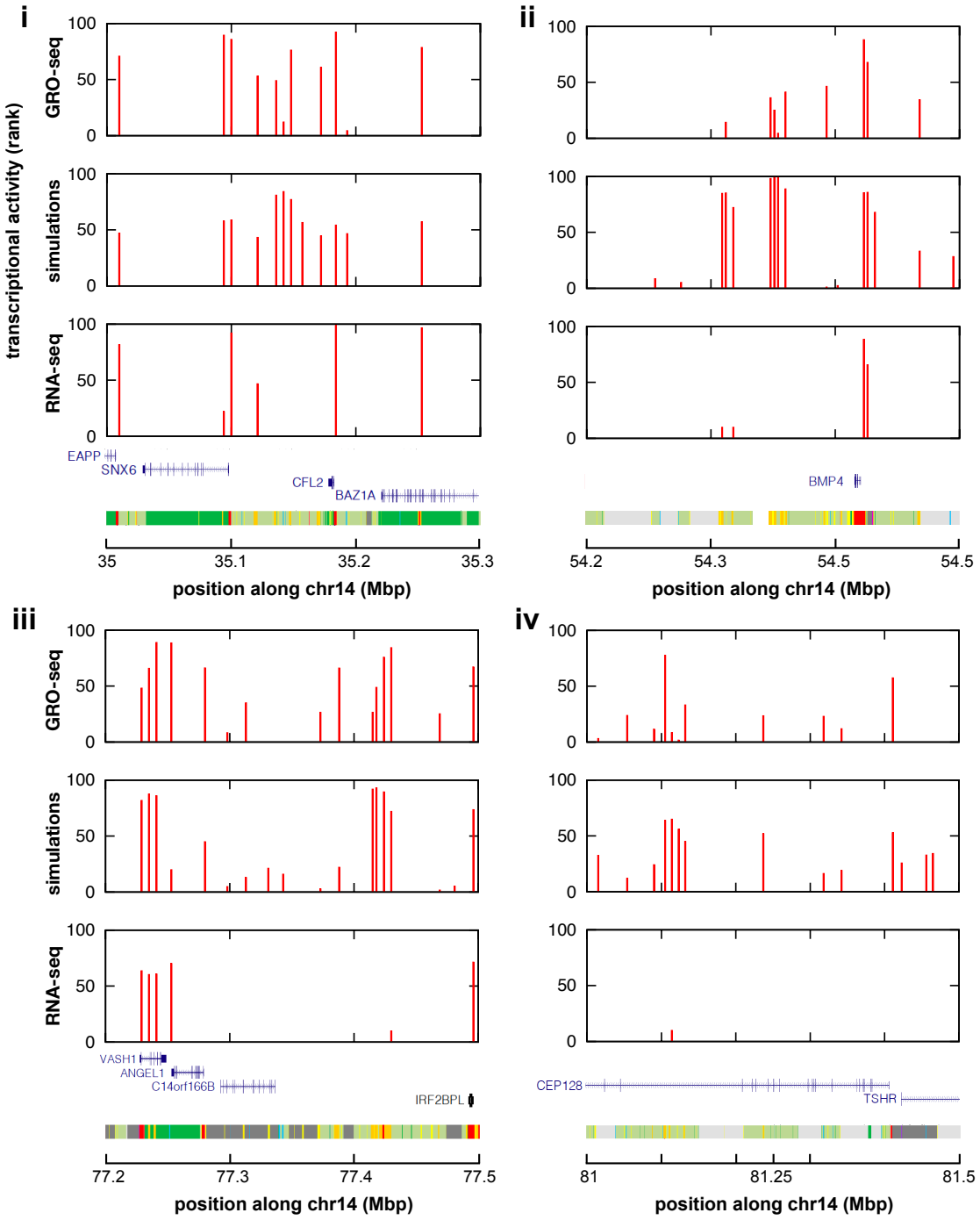

Supplementary Figure 6: **Comparison between transcriptional activity patterns in GRO-seq, simulations and RNA-seq. (i-iv).** The three tracks on each of the panels correspond to GRO-seq (top track), simulations (DHS model, middle track) and poly(A)$^+$ RNA-seq (bottom track) for 4 regions of chromosome 14, in HUVECs. To ensure the signals on the y axis have the same scale, we plot the rank of transcriptional activity of DHS beads. The rank is computed over all DHS beads in chromosome 14; for GRO-seq and RNA-seq, we remove data with no signal when computing ranks. The two tracks at the bottom of each panel correspond to the UCSC gene track (without non-coding genes and splice variants), and to the chromatin HMM track [3] for HUVECs. The RNA-seq dataset used was GEO: GSM2072428 [4]. The legend for the colours in chromatin HMM track is as follows [3]: bright red = active promoter; light red = promoter flanking; purple = inactive promoter orange = strong enhancer; yellow = weak enhancer; blue = CTCF/insulator; dark green = transcription; light green = low activity; gray = polycomb repressed; light gray = heterochromatin.

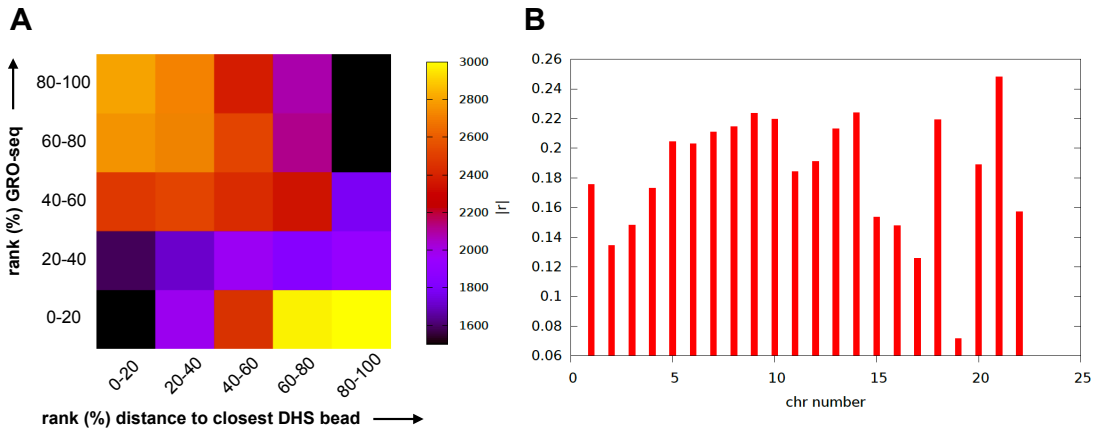

Supplementary Figure 7: **GRO-seq data inversely correlate with distance to nearest DHS peak, and the correlation varies genome-wide. A.** Correlation between the distance to the nearest DHS peak and the GRO-seq signal at DHS peaks genome-wide (ranked from $0-100\%$, then binned in quintiles and shown as a heat map). The heat map shows there is a negative correlation between the two quantities (range in the colour map reduced to highlight the pattern), analogously to the anti-correlation found in our simulations (see Fig. S1) and main text. **B.** The plot shows the absolute value of the Spearman correlation, $|r|$, between GRO-seq and the distance to the nearest DHS peak, for each chromosomes. The negative correlation is typically highly statistically significant: $p < 10^{-12}$ for all chromosomes except 16, 17, 19, 22, for which $p \simeq 5 \times 10^{-12}$, 5×10^{-12}, ~ 0.0007, 4×10^{-8} respectively. To compute the correlations, we coarse grain the GRO-seq data and DHS peaks into 1 kbp segments.

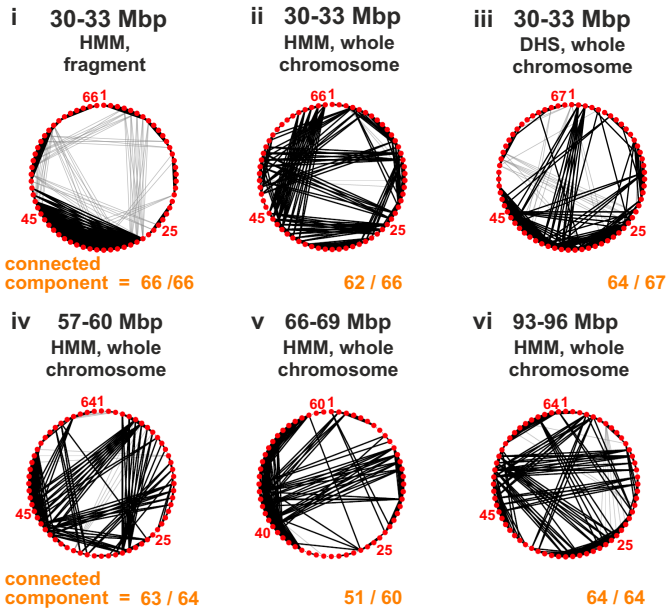

Supplementary Figure 8: **Regulatory networks in chains representing fragments of human chromosome 14 in HUVECs are highly connected.** Networks are constructed and presented as for Fig. 3 in the main text; they involve Pearson correlations between transcriptional activities of all TUs/red beads. To facilitate comparison with results in Fig. 3 in the main text, four fragments of the chain representing chromosome 14 are selected that have the same length as the 3 Mbp chain (Fig. 3 in the main text), and roughly the same density of TUs. (i) Dilute conditions (volume fraction $< 0.1\%$). Simulations (800 runs) involve a short 3 Mbp chain in a cube under the dilute conditions used for the 3 Mbp fragment simulations (as Fig. 3 in the main text), but with beads coloured using the HMM model (as Fig. 7 in the main text). Consequently, the statistical certainty associated with this panel is inevitably higher than in the other panels as $\geq$ 8-fold more runs are involved. (ii-vi) Confined conditions (volume fraction $\sim 14\%$). Simulations (100 runs) are conducted using the DHS and HMM models, and a string representing the whole chromosome in an ellipsoid (as Fig. 7 in the main text, and Fig. S5). Networks in all panels are highly connected. Comparison of panels (i) and (ii) – which allow comparison of the effects of confinement – points to confinement increasing the number of distant positive correlations (as might be expected). Comparison of panels (ii) and (iii) which allow comparison of the HMM and DHS models highlights the different patterns of marks contained within the two models. Comparison of panels (ii)-(vi) shows different segments of the chromosome have highly-connected components.

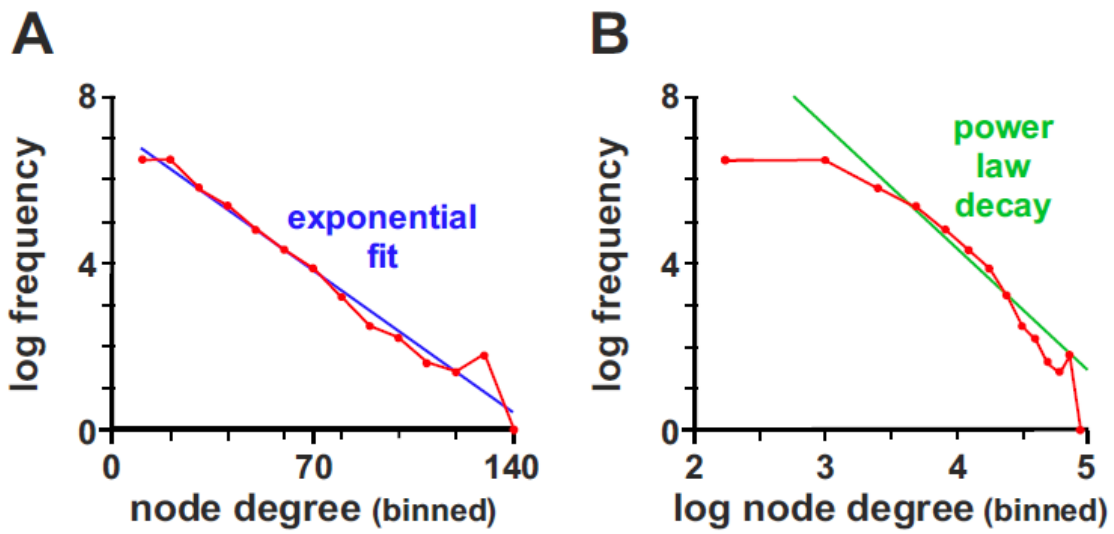

Supplementary Figure 9: **Node-degree distribution for transcriptional networks emerging from simulations (HMM model, HSA14, HUVECs).** An edge between two nodes is drawn when the Pearson correlation between corresponding TU beads is more than 0.35 in absolute value. **A.** Log-linear plot. The blue solid line is a linear fit, corresponding to an exponentially decreasing node-degree distribution. **B.** Log-log plot. The green line is a linear fit for intermediate node degree, corresponding to a power-law decay in the node-degree distribution (expected for a scale-free network). The power-law fit is poorer than the exponential one in (A).

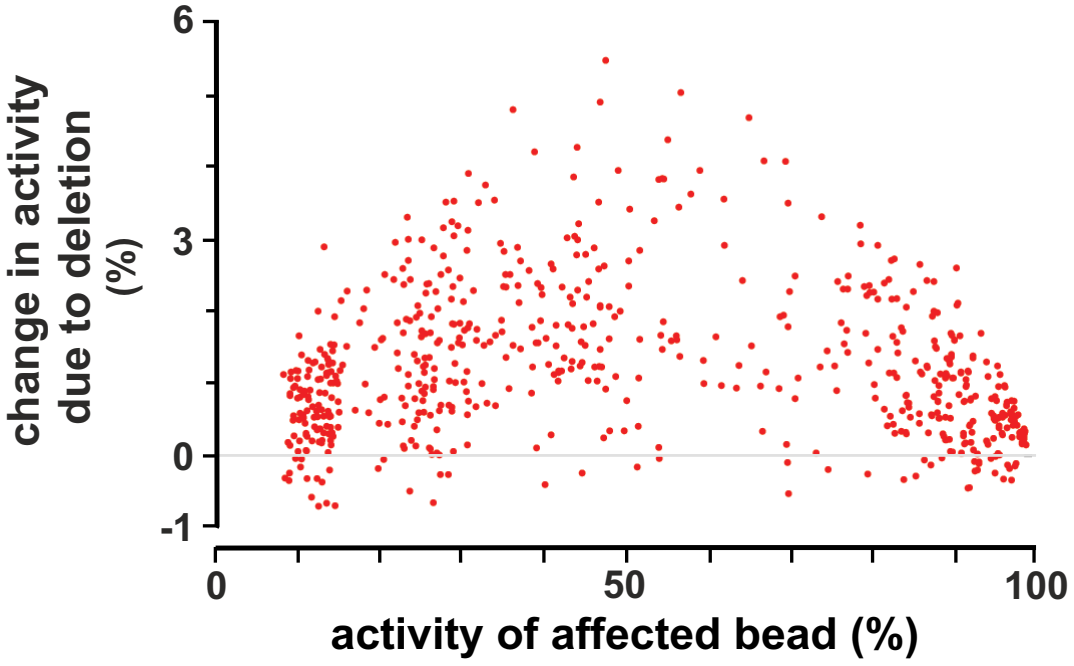

Supplementary Figure 10: **Change in transcriptional activity versus TU activity for DiGeorge deletion.** For each TU, we compute both the change in transcriptional activity in the chromosome 22 deletion studied in Fig. 8 in the main text, as well as the average transcriptional activity in the wild-type and deletion. This scatter plot shows that the change is larger for TUs with intermediate activity.

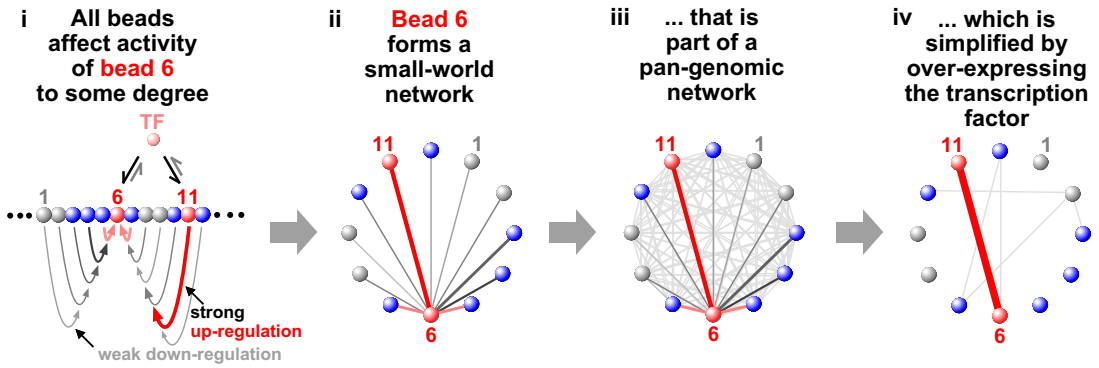

Supplementary Figure 11: **A pan-genomic model for transcriptional organisation and gene regulation.** (i) A region of the human genome is depicted with 12 segments (grey – heterochromatin, blue – open chromatin, red – transcription unit). TFs (transcription factor – polymerizing complexes) are present at non-saturating concentrations; they bind tightly to TUs *6* and *11*, weakly to blue segments, and not to heterochromatin. All other beads in the chain influence transcription of bead *6*. They can be considered as eQTLs acting on bead *6*, with eQTL strength being indicated by curved arrows (red – up-regulation, grey – down-regulation; increasing width/colour indicates increasing strength). (ii) The regulatory network centred just on bead 6. Straight lines indicate interaction strength (colour code as i). (iii) The regulatory network of all 12 beads. Every bead has some effect on the transcription of every other bead, which is consistent with GWAS results. (iv) Increasing TF copy-number (as in reprogramming experiments [5]) simplifies both the network of bead *6*, and the complete network. Consequently, over-expressing the TF over-rides the regulatory network mediated by 3D structure, and allows the coexisting trans-acting network envisioned by the omnigenic model to dominate.

Supplementary Note 1: Artificial chromatin fragment simulations

For the 3 Mbp chromatin fragment simulations, chains are made of 1000 beads (so that each bead corresponds to 3 kbp). For the simulations shown, TUs were placed at beads 2, 33, 49, 103, 105, 117, 129, 133, 146, 158, 233, 307, 316, 396, 404, 444, 457, 471, 508, 529, 584, 632, 645, 648, 661, 679, 685, 693, 718, 762, 795, 831, 886, 905, 907, 930, 931, 953, 979. Different simulations with different TU bead locations (randomly scattered along the fibre with average distance between 10 and 40) give qualitatively similar results, equivalent to the ones shown in the main text. The linear TU density in our simulations (between on average one bead in 20 and one in 40, or between 0.025 and 0.1) encompasses the range relevant to human chromatin. For instance, our whole chromosome simulations of HSA14 and HSA22 (see next Section) correspond to an average TU density (equivalently, density of 3 kbp bead corresponding to DHS peaks) of ~ 0.06 and ~ 0.04 respectively. The ratio between the number of active TFs, n, over the number of TUs, N, which we consider vary between 0.26 and 2.06, with most results presented for the former case. For this case, TFs are not enough to saturate TUs, which is the realistic case (see next section).

To start simulations, the chromatin fibre is initialised as a random walk, and proteins are initialised at random position within the simulation box – a cube of size 100σ, which means the system is dilute. To avoid bead overlap, we initially perform a small number of steps with a soft potential between beads, and a harmonic bond between neighbouring beads. We then equilibrate the system for 10^4 Brownian times with repulsive (WCA) interactions between any pair of beads. Finally we study the evolution of the system for 10^5 Brownian times (10^6 Brownian times for Fig. 2 in the main text) once the attractive Lennard-Jones interactions between chromatin beads and TFs are included in the potential.

The main parameter determining qualitative behaviour is the ratio n/N (number of active TFs to number of TUs). The magnitude of the attractive interaction between TFs and TUs and switching rate do not affect results qualitatively, provided the bridging-induced attraction drives clustering (i.e., we always get variable TU activity, stochasticity at the single-cell level and pangenomic transcriptional regulation dependent on 3D structure). The magnitude of low-affinity interactions, the interaction range r_c, and the persistence length of the chromatin fibre all affect transcriptional patterns and interactions quantitatively, but do not modify qualitative trends.

Supplementary Note 2: Transcriptional difference

To determine the difference between two sets of simulations in Figure 4 in the main text, which we refer to as states (typically corresponding to two different parameter sets), we define a transcriptional difference as follows. If there are N TU beads in the polymer, let us call x_i the expression (transcriptional activity, in %) of the

i-th TU bead in the first state, and x'_i its expression in the second state. The transcriptional difference between the two states is then

$$d_T = \sqrt{\sum_{i=1}^{N} (x'_i - x_i)^2}, \tag{S1}$$

which is the Euclidean distance between the two points $\{x_1, \cdots, x_N\}$ and $\{x'_1, \cdots, x'_N\}$ in their N-dimensional space.

Supplementary Note 3: Whole chromosome simulations

To simulate HSA 14 and HSA22 in a diploid G0 HUVEC cell, the system is confined into an ellipsoidal territory with aspect ratio chosen according to typical experimental values [6, 7] (semiaxes were 22.24σ:34.24σ:41.80σ, or 0.67 μm:1.03 μm:1.25 μm, for HSA14; 17.39σ:26.77σ:32.68σ, or 0.52 μm:0.80 μm:0.98 μm, for HSA22). Confinement is enforced by modifying the source code in LAMMPS to describe an ellipsoidal indenter. This introduces a soft force towards the centre of the ellipsoid, only if beads exit the confining ellipsoid. The magnitude of the confining force felt by a bead at position vector (x, y, z) is

$$f = K_g \delta g^2 \tag{S2}$$

for $\delta g > 0$, where

$$\delta g/a = \sqrt{x^2/a^2 + y^2/b^2 + z^2/c^2} - 1 \tag{S3}$$

where a, b and c are the semiaxes (along x, y and z), and where we assume for simplicity that the centre of the ellipsoid is in $(x, y, z) = (0, 0, 0)$. The constant K_g measures the stength of the confining force and is set to $10 k_B T/\sigma^2$. As a detail we note that the confinement is modelled via an effective force, rather than via an effective potential. Polymer size (in beads) for the simulated chromosomes are 35784 for HSA14, 17102 for wild-type HSA22, and 16250 for HSA22 with diGeorge deletion (again, each bead corresponds to 3 kbp).

There are about $50000 - 60000$ Pol II molecules in a diploid cell [8], corresponding to a ~ 2 nM concentration for a nucleoplasmic volume of ~ 520 μm^3 (a spherical nucleus of diameter 10 μm). FRAP shows that about a quarter of the Pol II molecules exchanges rapidly [9] and are likely to be active at any time. To reflect this, we consider 1700 and 813 TFs for HSA14 and HSA22 simulations respectively (in HUVEC cells), with $k_{\rm off} = 4k_{\rm on} = 0.001\ \tau_{\rm B}$, so that 20% of these are active on average at any time. As the number of TUs in our DHS model is respectively 2226 (HSA14) and 687 (HSA22), the value of n/N (ratio between average number of TFs active at any time and number of TUs) is ~ 0.15 (HSA14) and ~ 0.24 (HSA22), similar to values considered in the toy model (see previous section).

Our DHS model is described in the main text. Our HMM model is based on the HMM Broad chromatin track [3], which classifies chromatin segments into 15 different states using a hidden Markov model (HMM) applied to a range of

epigenetic marks (Suppl. Fig. S5). Here, states 1, 4, 5 – marking strong promoters and enhancers – are colored red (strong binding), while states 9, 10, and 11 – marking other transcribed regions – are blue (weak binding).

To start simulations, the chromatin fibre is again initialised as a random walk, with soft potential used to avoid overlap. The resulting self-avoiding chain is confined into the ellipsoidal territory quickly, analogous to what is done to create fractal globule structures. We additionally equilibrated the system for 10^4 Brownian times with repulsive (WCA) interactions between any pair of beads, before turning on the protein-chromatin interactions (after which again we collect data for 10^5 Brownian times). While this protocol is not sufficient to reach equilibrium for this long polymer [10], the fractal globule-like structure we choose for the initialisation corresponds to the one normally associated with interphase chromatin [11]. Additionally, as transcriptional activity depends on cluster formation which is predominantly associated with local chromatin folding – a much faster process than global folding [12] – we do not expect the initial condition to affect our conclusions and results. For instance, the chromosome fragment simulations start from an equilibrium configuration (see above), and the main results are qualitatively in line with those of the whole-chromosome simulations.

Supplementary Note 4: Quantification of small-world-ness

To quantify small-world-ness of a network, we use one of the approaches described in [13]. Thus, we create a number (typically 100) of randomised networks where the same number of edges as in the original network are randomly assigned to a a node pair. For both the original and the randomised network, we then compute: (i) the average over nodes of the clustering coefficient [14], which measures how close the neighbours of a node are to forming a clique, or a fully connected graph, and (ii) the average shortest path between a node pair. We call the average clustering coefficients γ and γ_r, for the original and a randomised network respectively, and the average shortest path L and L_r, for the original and a randomised network respectively. The small-world-ness can then be defined as $s = \frac{\gamma}{\langle\gamma_r\rangle}\frac{\langle L_r\rangle}{L}$, where $\langle\cdot\rangle$ denote averaging over many randomised networks. A value of $s > 1$ signals a small-world network. It should be noted that s can only computed with this definition for connected networks, for which L and L_r are well defined.

For the neworks in Fig. 3 of the main text, $s \simeq 1.90$ for $n = 10$ and $s \simeq 2.94$ for $n = 20$ (other networks are not connected). For chromosome 14, $s \sim 1.13$ for the DHS network (with threshold on absolute value of correlation 0.2 to draw an edge between a pair of nodes), and $s \sim 1.27$ for the HMM network (with threshold 0.2). For chromosome 22, $s \sim 6.63$ for the DHS networks and $s \sim 2.29$ for the HMM network (both with threshold 0.2). Therefore, all the networks we can characterise are small-world; it would be interesting to further probe changes in s with n/N and with chromosome region, and to understand the reasons for any significant pattern in the changes in s genome-wide.

Supplementary Note 5: Genomic datasets used

In this Section we detail the genomic datasets used to prepare inputs and compare

outputs in simulations of chromosome HSA 14 and 22 (Figs. 7, 8 in the main text and Suppl. Fig. S5).

Inputs to color beads in the DHS model are based on DNase-hypersensitivity (DHS) and H3K27ac peaks for HUVECs and hESCs, from ENCODE. Beads containing a peak in H3K27ac but not in DHS are colored as low-affinity (blue) beads, and those containing a peak in DHS are colored as high-affinity (red) beads. Beads which did not contain any peak (either DHS or H3K27ac) are colored as non-binding (gray). To color beads in the HMM model (HUVECs only), we use the chromatin states in [3] as detailed in Supplementary Note 3. Our simulations are based on the GRCh37-hg19 genome assembly for inputs.

To compare the predicted transcriptional activity of chromosome 14 outputted by our simulations with experiments, we use GRO-seq data. For HUVECs, we use the datasets GEO: GSM2486801, GSM2486802, GSM2486803 [15]; for hESCs, we use GEO: GSM1579367, GSM1579368 [16]. Super-enhancer regions considered here are those identified in [17], and available in the dbSUPER database, which includes super-enhancers for human and mouse cells.

Supplementary References

[1] Chris A. Brackley, Stephen Taylor, Argyris Papantonis, Peter R. Cook, and Davide Marenduzzo. Nonspecific bridging-induced attraction drives clustering of dna-binding proteins and genome organization. *Proc. Natl. Acad. Sci. USA*, 110:E3605–E3611, 2013.

[2] Chris A. Brackley, James Johnson, Steven Kelly, Peter R. Cook, and Davide Marenduzzo. Simulated binding of transcription factors to active and inactive regions folds human chromosomes into loops, rosettes and topological domains. *Nucleic Acids Res.*, 44:3503–3512, 2016.

[3] Jason Ernst, Pouya Kheradpour, Tarjei S Mikkelsen, Noam Shoresh, Lucas D Ward, Charles B Epstein, Xiaolan Zhang, Li Wang, Robbyn Issner, Michael Coyne, et al. Mapping and analysis of chromatin state dynamics in nine human cell types. *Nature*, 473:43, 2011.

[4] ENCODE Project Consortium. An integrated encyclopedia of dna elements in the human genome. *Nature*, 489(7414):57–74, 2012.

[5] Kazutoshi Takahashi, Koji Tanabe, Mari Ohnuki, Megumi Narita, Tomoko Ichisaka, Kiichiro Tomoda, and Shinya Yamanaka. Induction of pluripotent stem cells from adult human fibroblasts by defined factors. *Cell*, 131(5):861–872, 2007.

[6] Yejun Wang, Mallika Nagarajan, Caroline Uhler, and GV Shivashankar. Orientation and repositioning of chromosomes correlate with cell geometry–dependent gene expression. *Mol. Biol. Cell*, 28:1997–2009, 2017.

[7] P. R. Cook and D. Marenduzzo. Transcription-driven genome organization: a model for chromosome structure and the regulation of gene expression tested through simulations. *Nucleic Acids Res.*, 46(19):9895–9906, 2018.

[8] P. R. Cook. *Principles of nuclear structure and function*. Wiley New York, 2001.

[9] Hiroshi Kimura, Kimihiko Sugaya, and Peter R Cook. The transcription cycle of rna polymerase ii in living cells. *J. Cell Biol.*, 159:777–782, 2002.

[10] Guang Shi, Lei Liu, Changbong Hyeon, and Dave Thirumalai. Interphase human chromosome exhibits out of equilibrium glassy dynamics. *Nat. Comm.*, 9(1):1–13, 2018.

[11] Leonid A Mirny. The fractal globule as a model of chromatin architecture in the cell. *Chromosome Res.*, 19(1):37–51, 2011.

[12] Davide Michieletto, Davide Marenduzzo, and Ajazul H Wani. Chromosome-wide simulations uncover folding pathway and 3d organization of interphase chromosomes. *arXiv preprint arXiv:1604.03041*, 2016.

[13] Mark D Humphries and Kevin Gurney. Network small-world-ness: a quantitative method for determining canonical network equivalence. *PLoS ONE*, 3(4):e0002051, 2008.

[14] Marcus Kaiser. Mean clustering coefficients: the role of isolated nodes and leafs on clustering measures for small-world networks. *New J. Phys.*, 10(8):083042, 2008.

[15] Henri Niskanen, Irina Tuszynskax, Rafal Zaborowski, Merja Heinäniemi, Seppo Ylä-Herttuala, Bartek Wilczynski, and Minna U Kaikkonen. Endothelial cell differentiation is encompassed by changes in long range interactions between inactive chromatin regions. *Nucleic Acids Res.*, 46(4):1724–1740, 2017.

[16] Conchi Estarás, Chris Benner, and Katherine A Jones. Smads and yap compete to control elongation of β-catenin: Lef-1-recruited rnapii during hesc differentiation. *Mol. Cell*, 58(5):780–793, 2015.

[17] Aziz Khan and Xuegong Zhang. dbsuper: a database of super-enhancers in mouse and human genome. *Nucleic Acids Res.*, 44(D1):D164–D171, 2015.